



# Improving microstructural quantification in FIB/SEM nanotomography



Joshua A. Taillon<sup>a,1,\*</sup>, Christopher Pellegrinelli<sup>b</sup>, Yi-Lin Huang<sup>b</sup>, Eric D. Wachsman<sup>b</sup>, Lourdes G. Salamanca-Riba<sup>a,\*</sup>

<sup>a</sup> University of Maryland, Materials Science and Engineering, College Park, MD 20742, United States

<sup>b</sup> University of Maryland Energy Research Center, Materials Science and Engineering, College Park, MD 20742, United States

## ARTICLE INFO

### Article history:

Received 31 October 2016

Accepted 28 July 2017

Available online 9 August 2017

### Keywords:

Focused ion beam

Scanning electron microscopy

3D reconstruction

Microstructure quantification

Triple phase boundaries

Tortuosity

## ABSTRACT

FIB/SEM nanotomography (FIB-*nt*) is a powerful technique for the determination and quantification of the three-dimensional microstructure in subsurface features. Often times, the microstructure of a sample is the ultimate determiner of the overall performance of a system, and a detailed understanding of its properties is crucial in advancing the materials engineering of a resulting device. While the FIB-*nt* technique has developed significantly in the 15 years since its introduction, advanced nanotomographic analysis is still far from routine, and a number of challenges remain in data acquisition and post-processing. In this work, we present a number of techniques to improve the quality of the acquired data, together with easy-to-implement methods to obtain “advanced” microstructural quantifications. The techniques are applied to a solid oxide fuel cell cathode of interest to the electrochemistry community, but the methodologies are easily adaptable to a wide range of material systems. Finally, results from an analyzed sample are presented as a practical example of how these techniques can be implemented.

© 2017 Elsevier B.V. All rights reserved.

## 1. Introduction

The first successful research implementation of FIB-*nt* was reported nearly 15 years ago [1]. The technique has become much more common as the adoption of combined focused ion beam – scanning electron microscopy (FIB/SEM) systems has increased, such that commercial vendors now typically advertise and sell software packages specifically used to acquire 3D data (some common packages are: *Auto Slice and View* [2], *Atlas 5* [3], *Mill and Monitor* [4], and *3D Acquisition Wizard* [5]). Generally, the 3D data acquisition process proceeds as follows [6]:

1. To acquire a stack of SEM images, the sample is tilted to an inclined angle, usually the same as the angular offset between the electron and ion beams.
2. Using the FIB, a large trench is milled around an area of interest to expose a “data cube” to be acquired, which is then placed at the coincidence point of the two beams (see Fig. 1).

3. Slices of the sample are milled in the *z* direction, and after each mill, an image is taken with the electron beam in the *xy* plane (at an angle).
  - a) If desired, chemical and/or structural information can also be obtained at each slice by collecting X-ray EDS spectrum images (EDS) or electron backscatter diffraction (EBSD) patterns as well [7,8].
4. The slice and image process is repeated using automation software supplied with the microscope in order to build up a 3D volume of data.

FIB-*nt* has been successfully used on a broad variety of sample types, meaning the methods presented in this work will be of use in a wide range of scientific fields. Inkson et al. [1] initially developed the FIB-*nt* methodology for examining FeAl nanocomposites, but it has since been used for 3D chemical analysis of alloys [9], microstructural characterization of Li-ion battery electrodes [10], and pore structure characterization in shale gas samples [11]. FIB-*nt* has seen extensive use in the microstructural investigation of solid oxide fuel cell cathodes and anodes [12–29], and in the characterization of many other materials (see Holzer and Cantoni [6] for a thorough review). These works feature exciting findings in a range of materials, but the majority are published with a focus on samples and applications, rather than on microscopic methodology. As such, there are often only scant descriptions of methodology, and a lack of details about specific methods

\* Corresponding authors.

E-mail addresses: [joshua.taillon@nist.gov](mailto:joshua.taillon@nist.gov) (J.A. Taillon), [riba@umd.edu](mailto:riba@umd.edu) (L.G. Salamanca-Riba).

<sup>1</sup> Present address: Material Measurement Laboratory, National Institute of Standards and Technology, Gaithersburg, MD, 20899, United States.

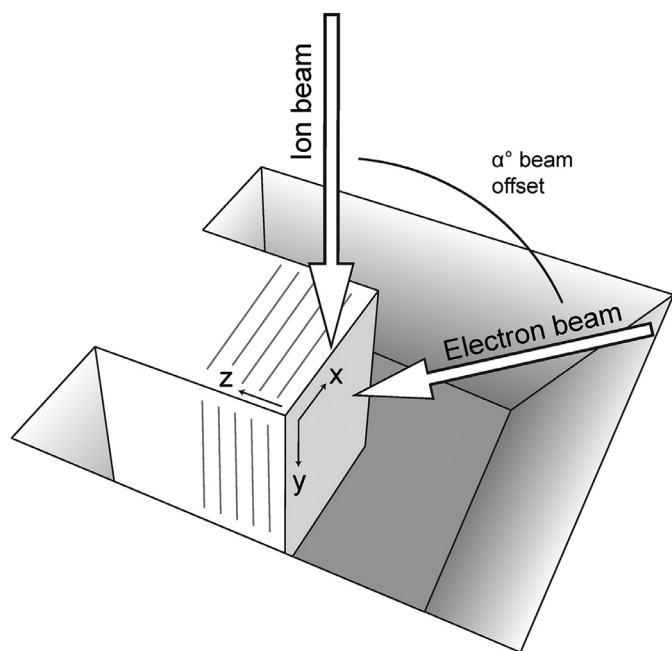


**Fig. 1.** Schematic of FIB-*nt* experimental geometry. The sample is positioned at the intersection of the electron and ion beams for simultaneous imaging and milling.  $\alpha$  is typically in the range of [50–55]°. Figure adapted from Holzer et al. [14].

and their implementations. In this work, we introduce and fully describe a number of techniques to improve the quality of acquired FIB-*nt* data. Our specific implementations are also published in a freely available repository to assist other researchers in the use and improvement of the methods presented here [30].

For the purposes of demonstration, the methods presented in this work are applied to a solid oxide fuel cell (SOFC) cathode sample. SOFCs are efficient and high-performance electrochemical energy conversion devices that are fuel flexible and cleaner than currently used alternatives [31]. On the cathode side of an SOFC device, the primary goal is the reduction of oxygen, which takes place at the boundary between the open pore, electrolyte, and cathode phase, known as the triple phase boundary (TPB). Accordingly, the morphology and three-dimensional microstructure of the cathode strongly affect the available sites for oxygen reduction, which in turn control the cathode polarization and performance.

More specifically, quantifiable microstructural parameters such as overall porosity, tortuosity ( $\tau$ ), and connectivity of the pore network have specific impacts on the total polarization resistance observed in the cathode. Other parameters such as surface area and volume of each phase change the available sites for gas adsorption within the cathode, while the triple phase boundary length controls overall charge transfer. Many of these parameters can be directly quantified using a FIB/SEM. The simplest parameters, such as porosity, phase surface area and volume, particle size, etc. were some of the first to be investigated using this method [14,15,17,18]. Wilson et al. [32] and Gostovic et al. [13] followed with detailed descriptions of phase and three-dimensional topological connectivity, respectively. Many authors have explored the concepts of phase tortuosity with various approaches, ranging from relatively simple center of mass considerations to more complex finite element modeling [13,16,20,21,32–34]. A natural extension of these methods was to examine the three dimensional interface between all phases (the TPB), and to quantify the total triple phase boundary lengths ( $L_{TPB}$ ), as well as the fraction of these that were expected to be electrochemically active [13,16,22,27,32,33]. In the SOFC literature (and in other fields as well), there is little consensus regarding the

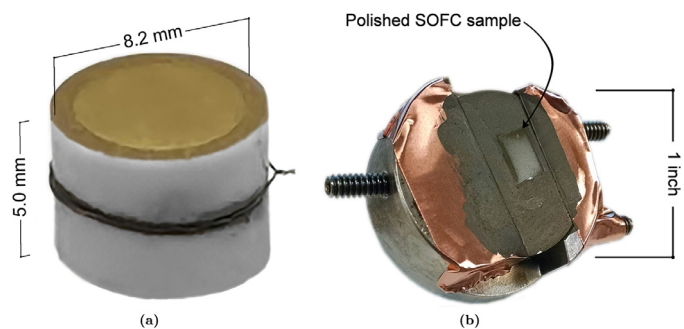


**Fig. 2.** (a) Photograph of half-cell SOFC stack. A Pt wire (for electrical measurements) is wrapped around the center of the (white) YSZ electrolyte support. The 30  $\mu\text{m}$  cathode layer is visible on the top of the support, and the entire top surface is coated with an Au contact. (b) Photograph of the SOFC mounted in cross section after epoxy impregnation, ready for FIB/SEM examination. The sample is mechanically clamped on the sides with three set screws.

methods used to measure many of these parameters. Even among works from the same research group, the specific techniques used to calculate  $L_{TPB}$  or  $\tau$  can vary widely (and the implementations are rarely publicly available), leading to difficulty comparing results between reports.

This work describes the specific techniques used to acquire a high resolution image stack from an LSM-YSZ composite SOFC cathode:

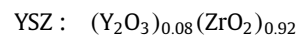


Image acquisition and post-processing strategies are demonstrated and discussed, followed by a detailed review of computational methods that can be used to calculate various morphological and microstructural properties from a three-dimensional dataset. Finally, implementation of these procedures is demonstrated on an example LSM-YSZ cathode sample.

## 2. Experimental procedures

### 2.1. Sample fabrication

An LSM-YSZ composite cathode layer was fabricated using standard screen printing techniques on a pre-sintered YSZ bulk electrolyte support, yielding an SOFC “half-cell”. For the support, YSZ powder (TOSOH Corp.) was uniaxially pressed in a 10 mm diameter die and sintered at 1450 °C for 6 h. The sintered electrolyte pellet was then polished to 5 mm thickness. Slurries of composite cathode material, made from 50:50 wt.% LSM-YSZ (Fuel Cell Materials), were screen printed onto the YSZ support, resulting in a cathode layer of approximately 30  $\mu\text{m}$ . The cathodes (together with the pre-sintered electrolyte) were sintered at 1100 °C for 2 h to remove the pore-forming material and generate a composite cathode layer with porous structure. A gold contact layer (for electrical measurements) was painted onto the surface of the cathode; a photograph of the cell is shown in Fig. 2a.

### 2.2. FIB/SEM sample preparation

The quality of a volume reconstruction can be only as high as each individual image that is acquired during the FIB-*nt* process. Many artifacts common to FIB/SEM can complicate the segmentation and reconstruction process, including (but not limited

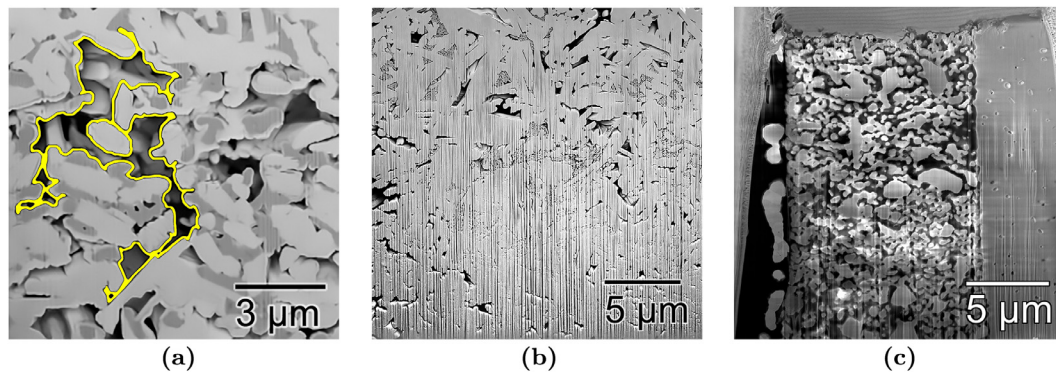


**Fig. 3.** Examples of common artifacts that can occur during a FIB/SEM nanotomographic acquisition. (a) The “pore-back” effect is the imaging of material that is not on the current plane of interest, which appears due to electrons escaping from the back of a pore through the open vacuum; (b) curtaining artifacts arise from ion channeling during the milling process and appear as vertical striations and (c) electron image ( $V_{acc} = 5$  kV) showing sample charging (bright regions) on a LSM/YSZ cathode that is typical when imaging poorly conducting materials.

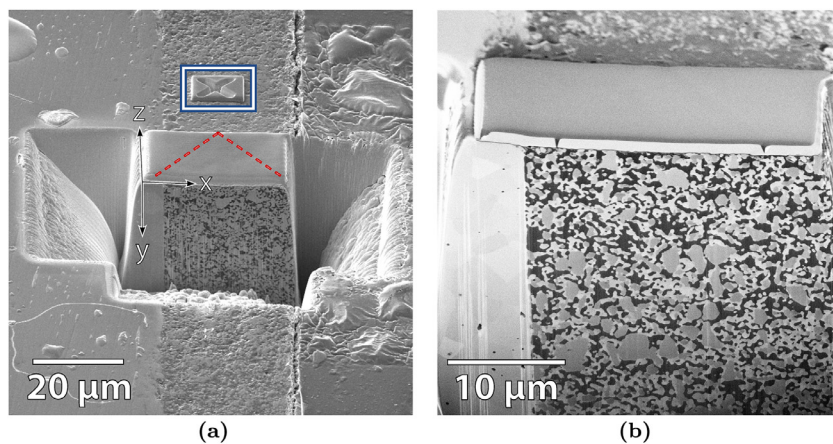


**Fig. 4.** (a) Overview of data acquisition site after initial preparation (trenching and fiducial milling). Referenced directions are as shown in the figure, such that each image is taken of an  $xy$  plane, and slices progress in the  $z$  direction (following the convention of Holzer et al. [14]). The dashed lines highlight the position of the lines milled into the protective layer to track slice thickness, and the outlined box is the fiducial mark that has been milled for ion beam positioning during the automated process. (b) Example raw image that is acquired during the FIB- $nt$  process. The bulk YSZ electrolyte is visible on the left, while the three phases (Pore – dark, LSM – intermediate, YSZ – bright) are all clearly distinguished in the composite cathode. The fiducials milled to measure slice thickness are visible in the FIB-deposited Pt at the sample surface.

to): “pore-back” imaging, FIB curtaining, and local sample charging. As such, a number of steps taken prior to SEM observation can significantly enhance the fidelity of the resulting volumetric representation, while other artifacts can be corrected through post-acquisition image processing.

Fig. 3 illustrates a few of the more critical artifacts encountered during an automated FIB- $nt$  acquisition. The “pore-back” effect is shown in Fig. 3a and is highlighted by the pore outlined in yellow. Within this region there is non-negligible contrast visible, arising from electrons emitted from behind the current face of interest that reach the electron detector through the open pore. While this feature is relatively easy to manually distinguish, this contrast causes significant challenges for automated segmentation routines, and is best avoided, if at all possible. Additionally, inhomogeneity in both surface and subsurface structure can result in ion channeling during milling, which causes vertical striations on the cut face (so-called “curtaining,” see Fig. 3b), preventing a clear view of the true structure at each slice. While any inhomogeneity can cause this effect, it is especially pronounced when there is open pore space, as the pores funnel the milling ions into specific channels. These artifacts can be somewhat mitigated by image post-processing [35], but initial avoidance is very beneficial to a high-fidelity reconstruction. Finally, electrical charging artifacts, which

are common in all SEM investigations of insulating samples (see Fig. 3c) [36], need to be mitigated as much as possible, especially in systems where subtle contrast changes are important (such as the LSM-YSZ composite imaged in this work).

Sufficient sample preparation and careful control of imaging conditions can alleviate many of the listed concerns. Both the “pore-back” and curtaining artifacts can be significantly reduced by impregnating the porous structure with a low viscosity epoxy. This makes the structure more homogeneous (reducing curtaining) and also prevents imaging of the pore-backs. Another option that achieves a similar effect with the benefit of added conductivity, is a Wood’s metal intrusion [37], although sensitive microstructures can be adversely modified by the pressure required to fill the pores. Careful consideration of specific sample requirements will determine the best procedure. Furthermore, these intrusion/impregnation strategies are only of use in samples with majority open pore networks, which provide a percolation pathway for the filling material.

In this work, a vacuum infiltrator (Allied VacuPrep) was used to fully encase the samples. The sample was placed in a 1 in. mounting cup such that the cathode-electrolyte interface was normal to the bottom surface. Samples were then degassed under vacuum for 5 min, at which point a low viscosity epoxy (Allied Epoxy-

Set) was flowed slowly over each cup, allowing ample time for the epoxy to fully permeate the porous structure. The epoxy was introduced using a 1/4" ID flexible tube, allowing approximately 1 drip (roughly 0.5 mL) per second. Once the samples were fully covered with epoxy, they were held under vacuum for 1 min and returned to atmospheric pressure, at which point they were left to cure overnight. Once cured, the samples were planarized using a low grit SiC abrasive paper (LECO). An automated polishing machine (LECO GPX-200) was used to grind the sample using 320–1200 grit papers, and then polished with a 3  $\mu\text{m}$  diamond suspension. To prevent charging, a thin layer (few nm) of carbon was sputtered (Balzers) onto the polished surface, and the sample was mounted with conductive graphite paint and Cu tape onto an epoxy mount SEM holder (Ted Pella, Inc.) (see Fig. 2b). Mechanical clamping of the sample is preferred over conductive adhesive mounting to maximize long-term acquisition stability and minimize physical specimen drift.

### 2.3. FIB/SEM observation

In this work, images for the three-dimensional reconstructions were obtained using an FEI Helios 650 dual beam FIB/SEM, at the Center for Nanoscale Science and Technology (CNST) user facility at the National Institute for Standards and Technology (NIST, Gaithersburg, MD). Once an area of interest is located, the surrounding area should be prepared to maximize the imaging signal and structural fidelity. First, a layer of protective Pt (or another material) is deposited on the sample surface using the ion beam. Next, two angled lines are milled into the deposited platinum, such that the thickness of each slice can be verified after acquisition<sup>2</sup> [38], on top of which a thick layer of protective carbon is similarly deposited. Different deposition materials are used to provide visual contrast between the layers, assisting the fiducial pattern tracking. Slightly above the area of interest, a fiducial pad (of carbon) is deposited, and a mark milled into it as a reference for the ion beam during the automated tomography process. Finally, a large "C-trench" is milled using the highest current to reveal the face of the desired data cube (see Fig. 4a).

Oftentimes in a 3D reconstruction, one is interested in segmenting two (or more) materials that are very similar in nature. Because of this, careful consideration of imaging parameters is necessary in order to optimize the contrast between the phases of interest, requiring the balancing of electron yield, interaction volume, and sample charging. While the specific settings will need to be tailored to various material systems, their discussion is included here in order to provide insight into the important practical considerations for FIB-*nt* data acquisition. In the composite cathode investigated in this work, the LSM and YSZ phases are often very difficult to distinguish owing to the similarity between and poor room temperature conductivity of the materials. Previous work on this system has revealed sufficient contrast can be extracted from these materials using low energy-loss backscattered electrons, collected using an energy filtered backscatter detector [33]. While this configuration was not available on the present tool, adequate (if not quite ideal) conditions were found using secondary electron imaging. The primary beam was low-energy, with an accelerating voltage ( $V_{\text{acc}}$ ) of 750 V, and was operated in the magnetic immersion mode. Detection utilized the "through the lens" detector (TLD) with a 600 V collection grid bias.

In addition to improving contrast between phases, the low  $V_{\text{acc}}$  improves spatial resolution and reduces the total interaction volume, enhancing the contrast within the epoxy-filled pores and providing sharper contrast at material edges. To prevent buildup of

charge within the specimen, images were taken using full frame integration of 16 images with a short (100 ns) dwell time per pixel. To improve the reliability of later quantifications, the field of view and resolution of the electron images were selected to result in approximately isometric voxel sizes (in this sample,  $\sim 20$  nm). Auto-focus and auto-contrast/brightness routines were performed before every image, resulting in raw images as shown in Fig. 4b. The assignment of particular intensity levels to each phase was confirmed prior to the full data acquisition using energy dispersive X-ray spectroscopy (EDS) scans (Oxford Instruments).

Once the site preparations were completed, the FIB-*nt* process was begun using the Auto Slice and View software (FEI Company). The prepared site was selected as the area of interest and the slice thickness was nominally set to 20 nm. Through post-acquisition analysis of the thickness tracking fiducials, the true slice thickness was determined to be  $20.0 \pm 0.3$  nm after approximately 40 slices were completed. Because earlier slices varied more in thickness as the beam approached the sample volume, slices taken prior to equilibration of the slice thickness were omitted from the analysis. In a typical acquisition, each slice required a total of approximately 2.5 min for milling and imaging. In the static geometry used here, no stage motion is necessary during the FIB-*nt* collection. For the dataset presented in this work, 605 usable slices were acquired during an approximately 28 h acquisition, yielding a total volume (after cropping) with  $x, y, z$  dimensions of (26.4, 19.9, 12.1)  $\mu\text{m}$ .

### 2.4. Data pre-processing

In addition to the methods used to acquire the image data, the processing steps that are taken can greatly affect the quality and fidelity of the resulting reconstruction. These processing steps are taken prior to image segmentation in order to facilitate the image labeling process and minimize the number of errors in the resulting output. In this work, these steps were implemented using a variety of software, including *Avizo Fire* (FEI Company), *Fiji* (open-source) [39], and Python libraries such as NumPy [40], OpenCV [41], and scikit-image (open-source) [42]. Where possible, other open-source libraries with similar functionality are recommended, although may not be specifically implemented in this work.

Collected images first require a shearing correction (in the  $y$  direction) to account for anisotropic voxel sizes in the  $x$  and  $y$  directions. This anisotropy is due to the foreshortening caused by the  $52^\circ$  angle of electron beam illumination. Additionally, although each image is acquired relative to a predefined fiducial marker, final alignment using a least-squares optimization (using the 'Align Slices' module in *Avizo Fire*, or the 'StackReg' plugin in *Fiji* [43]) will remove any residual artifacts from errant drift correction. Following alignment, the volume is then cropped to the area of interest within the acquired data.

Additionally, an intensity gradient is often observed on the acquired slices, due to the shadowing (lower detection efficiency) of electrons originating from the bottom of the sample face (see Fig. 5a). The shadowing artifact derives from the geometry of the system, and is a common issue in FIB-*nt* acquisitions that can complicate analysis [23]. Previous researchers have attempted to remove this artifact by changing the sample geometry. One method in particular, the block lift-out technique, has been demonstrated to be very successful, but requires a great deal of time (6 h to prepare a  $20 \times 20 \times 20 \mu\text{m}^3$  volume prior to any data acquisition) [6,44]. The shadowing in Fig. 5a causes an overlap within the global histogram between the brightest (YSZ) and moderate-intensity (LSM) phases. Bright pixels towards the bottom will be incorrectly grouped with the moderate pixels towards the top, which greatly hinders the segmentation procedure. While the darker portions at the bottom of the images could be cropped to remove the artifact

<sup>2</sup> See the FIB-SEM/fibtracking module of [30].

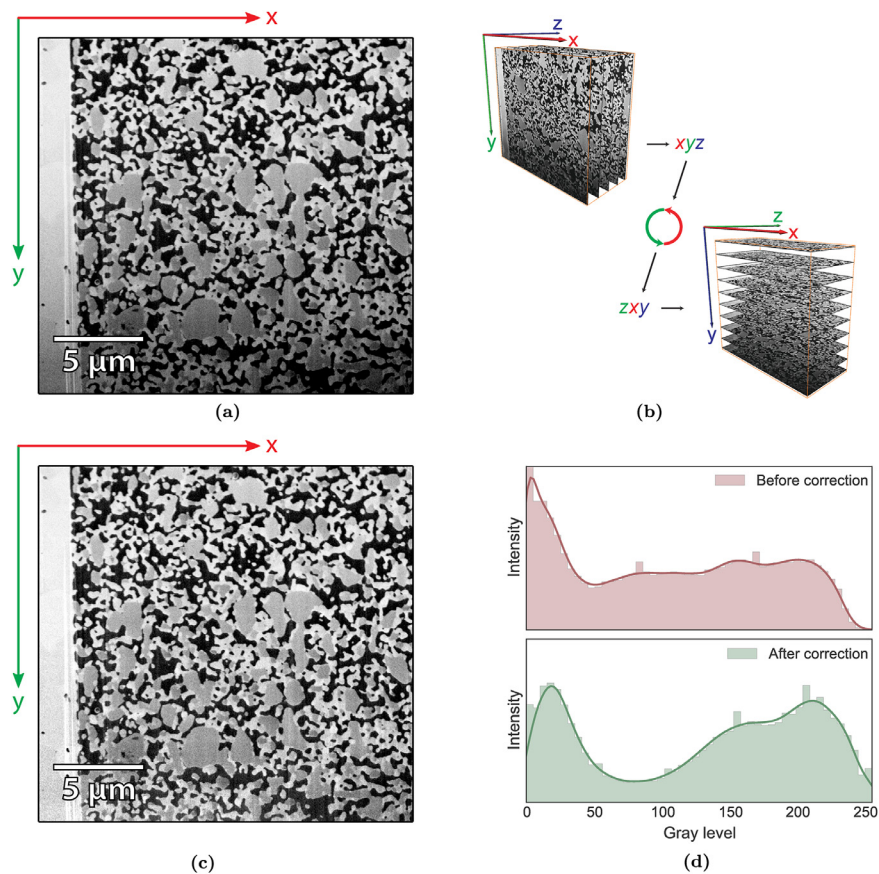


**Fig. 5.** Example of an acquired image (a) before and (c) after FIB trench shading normalization. (b) Shows the “reslicing” of the sample volume that enables the normalization. (d) Histogram and kernel density estimate for each image. After shading correction, the image is no longer undersaturated, and there is greatly improved contrast between the three phases, evidenced by the emergence of clearer intensity peaks (although still overlapping). In particular, much of the illumination in the [50 – 100] range (top, red) has been corrected into the pore and LSM peaks at 20 and 160, respectively (bottom, green). All images are displayed on the same brightness/contrast scale. (For interpretation of the references to colour in this figure legend, the reader is referred to the web version of this article.)

(at the expense of the total reconstructed volume), a correction mechanism is preferred to quickly enable full use of the acquired data.

A unique method to correct the intensity gradient observed in the images is presented in Fig. 5. The technique relies on the fact that the intensity gradient is relatively constant on successive slices in the  $z$ -direction and is only present in the  $y$ -direction. By “reslicing” the image data onto an orthogonal set of  $xz$ -planes, the gradient can be easily corrected. The original ( $xy$ ) images will have a gradient, but  $xz$  images will have uniform illumination on each slice and get progressively darker as the stack progresses in the  $y$ -direction (Fig. 5b). Each successive  $xz$  image can be normalized to the first by matching the first and second order statistics of the images’ probability distribution functions [45]. This normalization along the  $y$  dimension effectively removes the intensity gradient once the data is resliced to its original orientation (compare Fig. 5a and c). While surprisingly simple, this method greatly improves the segmentation results by reducing the amount of pixel-intensity overlap between adjacent phases (Fig. 5d) [30].

Finally, after all corrections are made, the images are filtered using a two-dimensional, edge-preserving non-local means filter implemented within *Avizo Fire* [46]. This filter is extremely effective at removing the noise present in FIB/SEM images while retaining the fidelity of edges between particles. Various open-source implementations of this algorithm are additionally available [47,48].

## 2.5. Image segmentation

As the number of phases present in a sample is increased, so is the complexity of an automated segmentation strategy. For a three-component system such as that in the present study, simple thresholding does not suffice to accurately label the particles contained within the volume. Manual intervention should also be kept to a minimum, for the sake of reproducibility as well as throughput. In this work, a marker-based watershed algorithm was used [49], implemented within *Avizo Fire*. The markers were set by using a conservative thresholding, such that only a fraction of the total volume is assigned to a phase. Each catchment basin is then filled according to the local gradient of illumination. This technique allows for a mostly automated process, requiring limited manual intervention to ensure that particularly challenging particles are correctly segmented. Final processing of the dataset involves restricted smoothing of the labels to reduce unphysically sharp corners, and the removal of small “island” particles, which may be formed by the presence of spurious single or few voxel labels. This segmented (binarized) dataset then formed the basis of the following quantitative analysis.

It should be noted that there is significant opportunity for advancement in this area. Current commercial solutions typically rely on simple thresholding (with *Avizo Fire*’s watershed implementation a notable exception) to label images into a segmented volume, often requiring extensive human interaction. A number of more advanced segmentation algorithms utilizing modern research

in the machine learning and computer vision fields have been presented in the literature (see [50–53]). Application of these methods to FIB-*nt* data could greatly facilitate the reconstruction process, and would improve one of the most difficult and time-consuming aspects of the technique.

### 3. Computational procedures

Once a segmented volume has been acquired, various microstructural parameters can be measured and calculated. In SOFCs, these values can then be directly related to cell performance. A number of these parameters have been well described in prior works [13,14,32], and as such will only be briefly reviewed here. A more detailed discussion is provided for the calculation of phase connectivity, phase tortuosity ( $\tau$ ), and triple phase boundary density ( $\rho_{\text{TPB}}$ ), as novel methods for these calculations were developed specifically during this work.

#### 3.1. Volume quantifications

##### 3.1.1. Phase volume fractions ( $\eta$ )

The volume and surface area of each phase can be calculated by generating a surface representation of each phase within *Avizo Fire* (analogous functionality is available using the *Blender* [54] or *VTK* [55] open-source software packages). Such routines create a network of triangles (mesh) to represent a particular phase with a three dimensional surface. Once the meshes are obtained, basic statistics for each phase can be calculated, including the total volume and surface area (in *Avizo*, this is accomplished with the ‘Surface Area Volume’ module), as well as the surface area to volume ratio (SA:V). The volume fraction for each phase can be obtained by dividing the volume of each phase by the total sample volume. This method of using a surface mesh is more accurate than a simple counting of voxels (used in prior works [18]), particularly for area calculations. This is because a voxel counting algorithm will overestimate the total surface area due to the discrete nature of the rectilinear voxel edges. For SOFC materials, solid fractions for each cathode phase ( $\eta_{\text{solid}}$ ) can be computed as the fractional volume for each solid phase (LSM and YSZ) relative to the total solid phase volume:

$$\eta_{\text{solid,LSM}} = \frac{V_{\text{LSM}}}{V_{\text{LSM}} + V_{\text{YSZ}}} \quad (1)$$

Comparing these ratios to those of the source materials enables an analysis of potential mass transfer from one phase to another during cell operation.

##### 3.1.2. Particle size ( $\bar{d}$ )

From the surface area and volume measurements, a global average of particle sizes can be determined through the use of a formula common in the Brunauer, Emmett, and Teller (BET) method, which measures powder sizes using gas adsorption techniques:  $D = 6 \times V/S$ , where  $D$  is the average particle diameter and  $V$  and  $S$  are the total phase volume and surface area, respectively [14,56]. This method assumes spherical particle geometry, which is generally an invalid assumption for these types of particles, but provides a simple means by which to compare the particle size magnitude of the various phases, and has been used in numerous prior FIB/SEM reconstruction studies [14,18–20,26,57]. If desired, further detail regarding the distribution of these parameters can be calculated as well, provided that individual particles can be suitably separated (which is not often the case for a very well percolated phase like those observed in the SOFC sample investigated in this work).

##### 3.1.3. Phase distribution

Phase distributions throughout each sample volume can be computed by examining profiles of the distribution in each orthogonal direction ( $x$ ,  $y$ , and  $z$ ). This is useful for investigating whether or not any anisotropic ordering is present within the phases. In this work, the distribution was calculated as the fraction of each plane that was occupied by each material along the profile direction. Within *Avizo*, this is accomplished using the ‘Volume per slice’ calculation available in the ‘Material Statistics’ module, but such a calculation would be relatively simple to implement in any other computing environment (e.g., *Python* and *NumPy*). In addition to viewing the phase distribution, the slope obtained by fitting a linear function to this profile allows for a measure of the magnitude of the change in  $\eta$  ( $\nabla\eta$ ), which can be compared between directions and samples. Variations in the phase distribution could imply migration of phases within the volume, and could have significant impacts on transport kinetics.

#### 3.2. Phase connectivity

The interconnectivity of different phases in a sample is a parameter that is often critical in determining the bulk transport properties and possible kinetic pathways of various reactions that may take place within it. A common technique to analyze this connectivity is to “skeletonize” the structure, making use of any number of possible algorithms [58]. The goal of these methods is to represent each phase by a graph that is homotopic (representative), thin (single voxel), and medial (at the center of the phase) [59,60]. In this work, *Avizo Fire* was used to calculate the skeletons (in particular, the ‘Distance Map,’ ‘Distance-Ordered Thinner,’ ‘Trace Lines,’ and ‘Evaluate on Lines’ modules). Using these individual modules (rather than the supplied “Auto Skeleton” feature) allowed for careful tailoring of module inputs to obtain a skeleton free of “starburst” artifacts, which are often produced using the default settings, especially in areas with large particles. Similar functionality is available in the *ITK* [61,62] and *CGAL* [63,64] libraries.

Using one of these techniques, the skeleton network for each phase can be calculated, and they each consist of one or more discrete *graphs*. Each graph in turn is comprised of a series of *nodes* that are connected by *edges*. A number of useful statistics regarding the network can be figured, many of which were first introduced in the SOFC literature by Gostovic et al. [13]. A brief overview of these metrics is provided here, and a simple illustration of each is given in Fig. 6 for reference. Useful among the quantifiable parameters are the number of edges ( $E$ ) and nodes ( $N$ ) within the skeleton network of each phase, as well as their volumetric density, relative to total sample volume ( $\rho_E$  and  $\rho_N$ , respectively). From these values, the degree of each node ( $k_i$ ) can be calculated by counting the number of edges coinciding at each node:  $k_i = E_i/N_i$ . The mean of these values ( $\bar{k}$ ) gives a measure of the amount of self-connectivity in each phase [13]. Finally, the mean topological length ( $\bar{L}$ ) defines the average distance throughout the network that can be traveled between branching nodes. Physically, this property can be interpreted as a sort of mean free path for particles traversing the network.  $\bar{L}$  is calculated by summing the lengths of each edge within the network ( $l_i$ ) and dividing by the number of nodes present:

$$\bar{L} = \frac{1}{N} \sum_i l_i. \quad (2)$$

In addition to these metrics from previous works, another useful measurement that can be obtained from the skeleton model is the degree of percolation for a phase ( $p$ ). This parameter aims to quantify the fraction of the overall skeleton network length that is interconnected (percolated). Each phase network (with total length  $L$  and mean topological length  $\bar{L}$ ) consists of a finite number of individual graphs (with lengths  $\mathcal{L}_i$ ), and each graph represents a

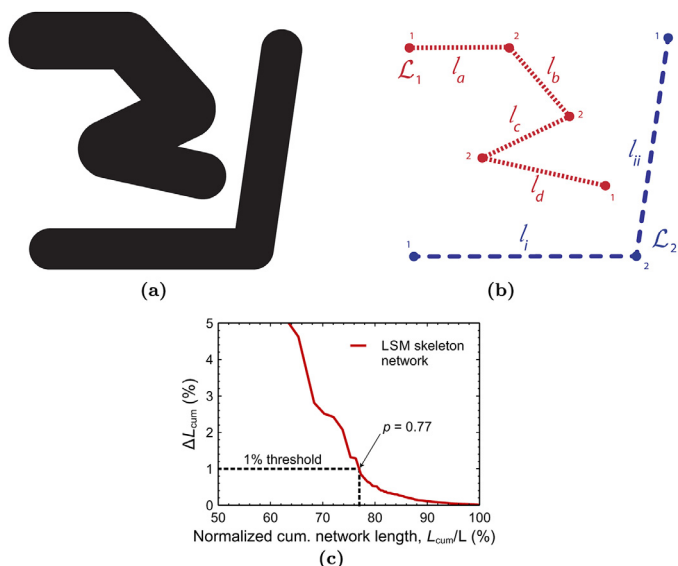


**Fig. 6.** (a) Artificial simulation of a 2D phase, consisting of two discontinuous components. (b) Theoretical skeletonization of the phase presented in (a). This total network consists of two graphs, with lengths  $\mathcal{L}_1 = l_a + l_b + l_c + l_d$  and  $\mathcal{L}_2 = l_i + l_j$ . In this simple example,  $N = 8$ ,  $E = 6$ ,  $\bar{L} = (\mathcal{L}_1 + \mathcal{L}_2)/8$ , and  $k$  for each node is represented by a small number adjacent to each node. (c) Example determination of the degree of percolation,  $p$ , for the LSM phase within the SOFC sample characterized in this work. The percentage change in cumulative network length  $\Delta L_{cum}$  is calculated, and the value of  $L_{cum}/L$  where  $\Delta L_{cum} < 1\%$  is taken as  $p$ .

portion of the total network that is discontinuous with the remainder of the network (see Fig. 6a and b for a simple example). If a phase is particularly discontinuous, its network will consist of many smaller graphs. A fully percolated phase on the other hand would be represented by one large graph. The degree of percolation ( $p$ ) is defined in this work by sorting the individual graphs by length and finding the point at which the cumulative network length changes by less than 1% as follows: The individual graphs (with lengths  $\mathcal{L}_i$ ) are sorted in decreasing order and their cumulative sum ( $L_{cum}$ ) is calculated. If the total length of the network is  $L$ , the value of  $p$  is taken to be the value of  $L_{cum}/L$  at the point where adding successive terms to  $L_{cum}$  cause a change ( $\Delta L_{cum}$ ) of less than 1%. Formally,  $p$  can be defined as:

$$p = \frac{\sum_n \mathcal{L}_n}{L} \quad \text{s.t.} \quad \frac{\mathcal{L}_{n+1}}{L} < 1\% \quad (3)$$

A  $p$  near unity represents a phase that is fully percolated throughout the sampled volume, while significant deviations correspond to poorly connected phases. An example determination of  $p$  is shown in Fig. 6c.

### 3.3. Tortuosity ( $\tau$ )

Another useful microstructural measure in these systems is the amount of tortuosity in each phase. In general, “tortuosity” ( $\tau$ ) is a rather poorly defined parameter [65], and is frequently determined differently for each particular case in question. At its essence however, tortuosity represents the added difficulty that a particle traveling through a phase experiences due to the complexity of the available physical paths (such as a gas molecule through the pore space). Among other properties, the degree of tortuosity can affect the ease of molecular diffusion and both electrical and ionic conductivity through a material [34]. As such, it is an important parameter to accurately quantify in any system poten-

tially limited by species transport, especially in SOFC cathodes and anodes.

Within the literature specific to SOFC electrode reconstructions, various methods have been used to calculate  $\tau$ . Generally,  $\tau$  can be calculated on a geometric, hydraulic, electrical, or diffusion basis [65], leading to disparate methods being used throughout prior works. Some of the earliest techniques were based on a Monte Carlo method, approximating molecular flux through a finite element model of the pore volume in an SOFC anode [16]. Vivet et al. [24] further expanded upon this method with a finite difference solution to the diffusive transport equation. Joos et al. [23] used a similar method to calculate electrical tortuosity, solving Ohm’s law on a finite element model to compare effective conductivities, the ratio of which was defined as the tortuosity.

Besides these application specific techniques, another set of methods are those based on purely geometric (*a.k.a.* geodesic) considerations. These methods are much simpler to calculate, and aim to describe purely the physical tortuosity of the microstructure. Because they do not rely on a material’s diffusivity or conductivity, the values obtained can be easily compared between different phases, materials, and samples, at the expense of a direct physical interpretation of the results. In short, the geometric tortuosity between two points is simply the ratio of the geodesic distance ( $L_G$ ) and the euclidean distance ( $L_E$ ) between them.  $L_G$  is the shortest path that is possible given the presence of any interfering structure (such as another phase), and  $L_E$  is what the shortest distance would be if there were no hindering structure (the “straight-line” distance or sample thickness).

Some of the first methods to calculate the geometric tortuosity relied on tracking the center of mass of each phase on each slice, and comparing the length of this path to the straight line distance through the sampled volume in the same direction [13,19]. This technique has since been made available in *Avizo* as the “Centroid Path Tortuosity” module. While simple to implement, this method has significant limitations in that it calculates the geodesic distance globally, rather than at every point within the volume. This results in the method being generally insensitive to local variations in structure, such as can arise from bottlenecks and phase discontinuities. Another approach to calculating the geometric tortuosity based on a diffusion-simulating random walk method has been used in the literature as well [22,66], providing both local and global information about tortuosity, but requiring significant computational effort.

In this work, a geometric approach to calculating tortuosity has been implemented. Unlike prior methods, it does not depend on computationally-intensive simulation, and  $\tau$  is calculated at every point within the volume, rather than on a global basis. Specifically, the definition of  $\tau$  used in this work is that provided by Gommès et al. [34], which has gained traction in recent literature (e.g. [67–69]):

$$\tau = \lim_{L_G, L_E \rightarrow \infty} \frac{L_G}{L_E} \quad (4)$$

where  $L_G$  and  $L_E$  are the geodesic and euclidean distances, respectively. Fig. 7 illustrates the method for a pore phase  $\tau$  calculation in the LSM/YSZ composite cathode. The geodesic distance (Fig. 7a) is calculated at every point throughout the volume using a Fast Marching Method (FMM) [70,71]. The euclidean distance (Fig. 7b) is calculated as a simple “straight-line” measurement, parallel to the particular direction of interest. The tortuosity (Fig. 7c) was then figured by dividing these values. While the true  $L_G \rightarrow \infty$  limit of  $\tau$  cannot be figured exactly due to the limited sampling volume, a representative average value for each direction can be obtained by computing the tortuosity profile (Fig. 7d) along each dimension. To reduce the impact of local oscillations in the profile, the mean and

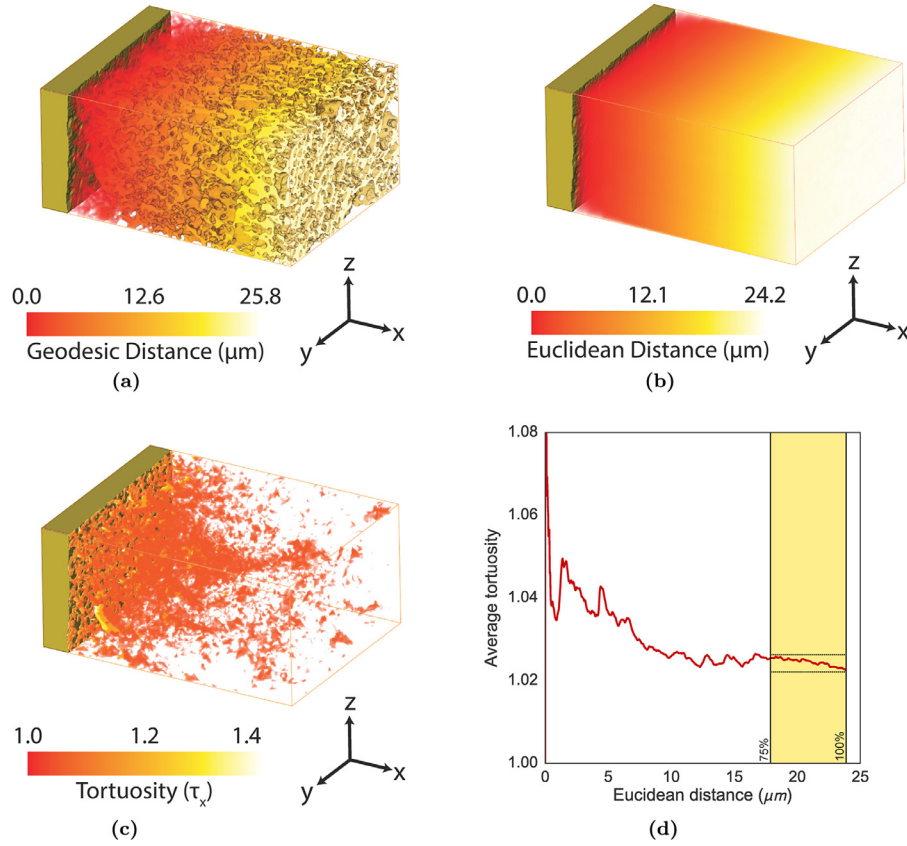


**Fig. 7.** Example of tortuosity calculation (in the  $x$  direction) for the pore space in an SOFC cathode sample. The (a) geodesic and (b) euclidean distances from the electrolyte/cathode interface are calculated for every voxel within the cathode volume. Dividing these values at every point yields (c) the tortuosity at every voxel. This data can be averaged into (d) a profile along any direction, in this case  $x$ , which is perpendicular to the interface of interest. The error of the measurement depends on the convergence (as a function of sampled volume), and is estimated as  $\pm$  one standard deviation of the data contained within the final 25% of the profile (as shaded above).

standard deviation of  $\tau$  within the last 25% of the profile (as highlighted in Fig. 7d) is reported as the value and error for  $\tau$ . As will be shown in Section 4, this technique correctly indicates significantly higher error in the measurements of  $\tau$  for phases with a large degree of discontinuity.

Of further interest in the specific application of  $\tau$  to SOFC samples is the ratio of volume phase fraction to tortuosity,  $\eta/\tau$ . This parameter is a determining factor for the effective diffusivity of gaseous molecules through the porous structure an electrode. The effective diffusivity due to the tortuous porous structure has been defined as

$$D_{\text{eff}} = \frac{\eta}{\tau} D \quad (5)$$

where  $D$  is the Knudsen diffusivity without the effects of porosity and tortuosity [72]. Using this ratio, relationships between the expected  $D_{\text{eff}}$  can be examined by measuring only two relatively simple microstructural properties.

### 3.4. Triple phase boundary density

In many multiphase systems, the distribution of the common boundaries between materials is critical in controlling the reactions that take place within a device, and contributes significantly to its overall performance. In electrochemical devices such as a composite SOFC cathode, the triple phase boundary (TPB) is a location where all three phases (cathode, electrolyte, and pore space) meet, and the three necessary reactants (electrons, ions, and gaseous oxygen) are present. The total network of TPB locations represent sites where  $\text{O}_2$  can be reduced according to the oxygen

reduction reaction (ORR):



allowing the air-side operation of the fuel cell. A direct relationship between the volumetric density of TPB points ( $\rho_{\text{TPB}}$ ) and SOFC performance has been previously observed [19,73], making the accurate quantification of this parameter of utmost importance. As such, a brief review (and evaluation) of some common methods, as well as a description of an improved implementation for the calculation of  $L_{\text{TPB}}$  are presented here.

#### 3.4.1. Existing methods

$L_{\text{TPB}}$  (and  $\rho_{\text{TPB}}$ ) have been quantified using numerous techniques, leading to some discrepancy between reported values, even for similar materials [33,74]. Among the techniques that have been used are phase change analysis, [19], intersection point analysis [13], theoretical simulation [74], stereology [75], voxel edge-counting [32], centroid smoothed edge-counting [21], and the volume expansion method [22,66]. As expected, the values produced by each of these methods vary based on the differences of the underlying techniques. Some of these methods (in particular the edge-counting methods) overestimate TPB lengths due to improper handling of the discrete nature of a three-dimensional voxel representation. The centroid smoothing algorithm, essentially a three-dimensional box filter, improves upon edge-counting by simulating a more physically realistic TPB path through the volume [21].

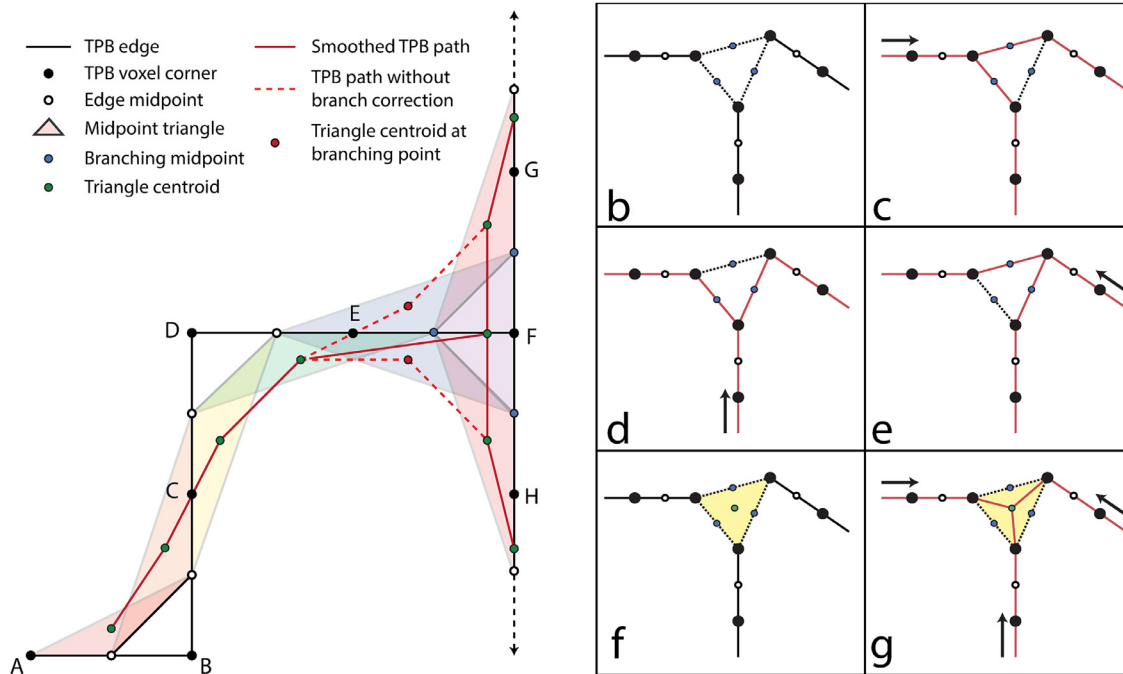


**Fig. 8.** (a) Schematic diagram of the centroid smoothing algorithm used to calculate the TPB network. The diagram is shown in two dimensions, but the concepts are easily extended to three. The black path ( $ABCD\dots$ ) depicts a theoretical path of TPB edges with a branch occurring at point F. The centroids of subsequent edges (green dots) are connected, and a new point is created at all branching points in order to preserve the topology of the original TPB network. The centroid smoothed network is represented by the solid red lines. The dashed lines represent how the network would be figured without correction of branching points. (b–e) Example of a branching TPB path and how the total length calculated will vary depending on the direction of approach when counting TPB edge lengths. (f) Addition of centroid at branching point. (g) TPB path determined using additional centroid. The total path length remains consistent regardless of direction of approach during the calculation. (For interpretation of the references to color in this figure legend, the reader is referred to the web version of this article.)

### 3.4.2. Implementation of a centroid edge counting method

In this work, a centroid smoothed edge-counting technique to measure TPB networks is presented. This method extends and improves the implementation presented by Shikazono et al. [21], and has been made publicly available.<sup>3</sup> An overview of the algorithm is presented in Fig. 8. Briefly, this algorithm operates on a segmented volume by finding the voxel edges (i.e. the edges of a cube) where the four neighboring voxels contain all three phases. The edges are joined into TPB paths to form a TPB network for each volume, which is then smoothed by a centroid box filtering process. Within the TPB path, the centroid of the triangles formed by voxel edge midpoints is used to determine the overall path. The filter is clamped at endpoints of a TPB path (such as A in Fig. 8a), such that the endpoint is used to fill the neighborhood where a midpoint is missing.

Additionally, the algorithm presented in this work has been optimized to include homotopic network descriptions at branching TPB points. Because of the branching points, the network could fail a self-consistency test if calculated multiple times starting from different points within the structure, as shown in Fig. 8c–e. A simple solution to this problem is to add an additional point at the center of each branch within the path. The center is determined by finding the centroid of the voxel edge midpoints surrounding each branch (Fig. 8f). Once this has been done at all branching locations, the TPB network is built by connecting the TPB paths as shown in Fig. 8g. This technique ensures that the total TPB length will be measured the same regardless of the direction from which the length is measured, and that the topology of the true TPB network is preserved.

### 3.4.3. Comparison to volume expansion method

Recently, a “volume expansion” method has gained favor within the literature as an alternative means by which to calculate the TPB network due to its computational simplicity. This method uses global morphological operations on each phase and does not require the traversal of the entire volume [22]. Briefly, the volume expansion method consists of three steps: a morphological dilation of the three phases that are present, a logical operation to find where the three phases overlap, and the thinning of the resulting volume to yield a three-dimensional network. While this method is more computationally efficient than an edge-counting algorithm, it relies on a number of configurable parameters that can significantly affect the resulting network. The direction, dimensionality and magnitude of the dilation all affect the morphology of the resulting overlapping volume, in addition to the parameters used in the algorithm to skeletonize the volume.

To examine these effects, a test volume was created as shown in Fig. 9. While the model is simplistic, it is effective in demonstrating some of the most important limitations inherent in the volume expansion method. It consists of two overlapping circles (with radii of 60 voxels) in the  $xy$  plane that have been extruded in the  $z$  dimension. The vertical position of the circles ( $y$ ) is determined by the arbitrary sinusoidal function  $y = 20 \sin\left(\frac{2\pi}{400}z\right)$ , resulting in an S-shaped volume (Fig. 9b). Each circle and the surrounding volume are considered a distinct phase, such that there are two TPB paths within the volume, each with a full period sine wave path with length 409.7 linear voxel units ( $lvu$ ), calculated by integrating the arc length of  $y(z)$ . Summing the lengths of the two paths gives an exact theoretical  $L_{TPB}$  of 819.4  $lvu$ . The volume expansion method was tested by repeating the TPB measurement on this theoretical volume using various dilation and skeletonization settings (Fig. 9c–e). Depending on the settings used, the length of the resulting TPB

<sup>3</sup> See the TPB scripts module of [30].

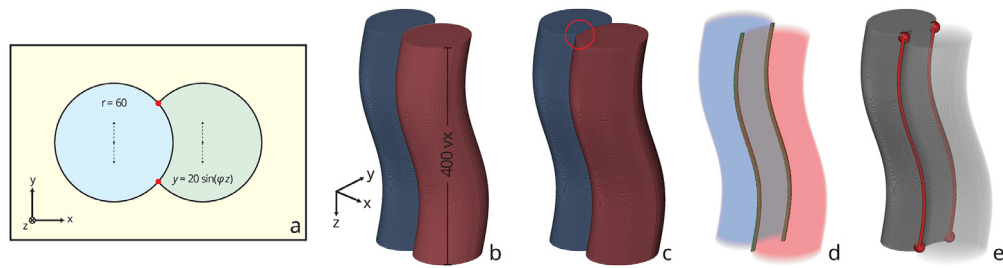


**Fig. 9.** Example of TPB test volume and volume expansion calculation method. (a) 2D template used to create test volume. The red dots highlight the TPB points in two dimensions. The positions of the two circles were oscillated together in the  $y$ -direction to generate (b), a 3D volume extruded in the  $z$ -direction. In this example,  $\varphi = \frac{2\pi}{400}$ , such that one period of the sine function was completed over the 400  $z$  voxels. (c) The original surfaces are dilated by four voxels in each of the six neighboring directions, causing the two cylinders to overlap one another by a small amount. Evidence of the overlap is visible in the area circled in red. (d) The overlapping volume of the dilated data is located at the interface between the two phases, as expected. (e) This volume is then skeletonized using typical thinning algorithms to yield the TPB network (shown in red). (For interpretation of the references to color in this figure legend, the reader is referred to the web version of this article.)

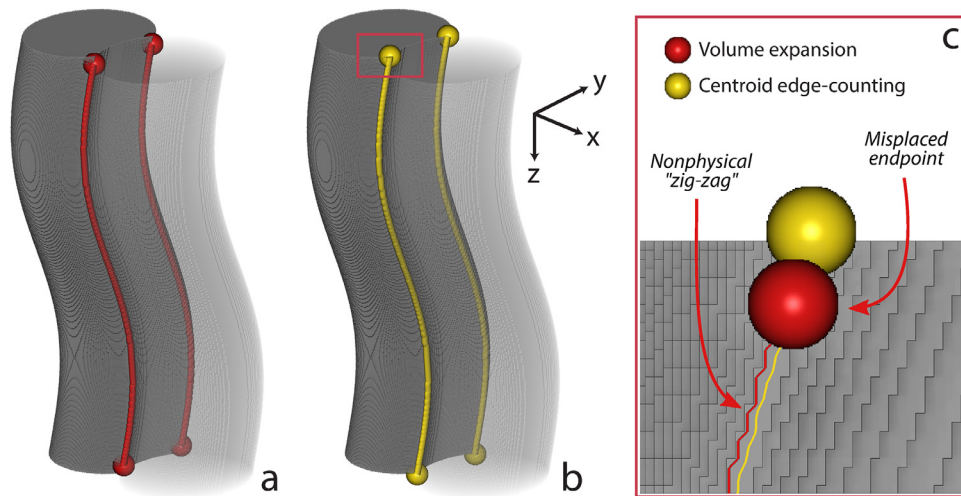


**Fig. 10.** Comparison of the two methods used to determine TPB network on the test volume described in Fig. 9. (a) TPB network measured using the volume expansion method (red, *color online*). Note, the “best-case” parameters were used in this figure, resulting in a measurement of 823.2  $lvu$  (0.5% error). (b) TPB network measured using the centroid edge-counting method (yellow, *color online*) gives a measurement of 820.9  $lvu$  (0.2% error). The outlined region is shown in detail in (c), demonstrating the differences between the two methods. Notice that for the centroid algorithm introduced in this work, the TPB path endpoint is properly located at the edge of the volume ensuring an accurate calculation of the total  $L_{TPB}$ . (For interpretation of the references to color in this figure legend, the reader is referred to the web version of this article.)

**Table 1**

Comparison of the centroid edge-counting and volume expansion methods used to calculate  $L_{TPB}$  for the sample volume of Fig. 9. Units of each value are  $lvu$ ; the percentage provided represents the degree of error compared to the true  $L_{TPB}$  value. For the volume expansion method, the minimum, mean, and maximum values obtained for a range of algorithm input parameters are reported.

Ground truth $L_{TPB}$	Centroid edge counting	Volume expansion
819.4	820.9 (0.2%)	Min: 814.5 (−1.2%)
		Mean: 834.6 (1.9%)
		Max: 880.4 (7.5%)

network was found to vary by up to approximately 9% (see Table 1). By contrast, the implementation of the centroid method presented in this work (which does not use “tunable” parameters) obtained almost the exact correct result, within 0.2% error of the true value.

A detailed comparison of TPB paths obtained with both the volume expansion and centroid edge-counting method is shown in Fig. 10. In Fig. 10c, the difference between the two methods is clearly seen. When used with the “best-case” parameters, the volume expansion method was able to approximate the theoretical  $L_{TPB}$  in this simple example, but it is clear that this is due to two distinct errors counteracting one another. First, the location of the TPB endpoints is incorrectly placed, as can be observed by the displacement of the red sphere from the top edge of the cylinder vol-

ume in Fig. 10c. Due to the volume dilation and then erosion, the phase microstructure is intentionally modified, and the exact position of the TPB path edge is lost. As such, the node at the end of the TPB path is not explicitly preserved at the phase boundary. This error serves to shorten the overall measured  $L_{TPB}$ , but is counteracted by the insufficient smoothing of the TPB network when generated by volume expansion. This is evidenced clearly by the unphysical “zig-zag” pattern that arises from the discrete nature of the voxel representation and is visible in Fig. 10c. This results in a wide range of possible values for the measurement, depending on the specific settings used for the morphological operations. In a real dataset, these small errors will be greatly magnified due to the large number of discrete TPB paths within the overall network. In fact, the range of  $L_{TPB}$  values obtained for one experimental dataset varied  $\pm 30\%$  depending on the settings used for dilation and skeletonization, indicating that while the volume expansion method may be suitable for simple structures, it is likely less appropriate for complex ones such as those observed in composite SOFC electrodes due to the convolution of multiple sources of error.

#### 3.4.4. Estimation of electrochemical activity

Of particular interest in the electrochemical applications of FIB-nt is a measurement of the expected “activity” of the different parts of the TPB network. Within a composite cathode, a certain

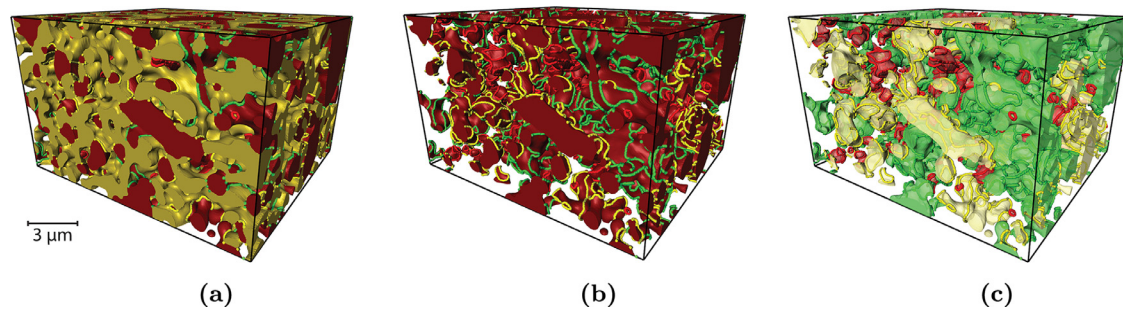


**Fig. 11.** Example classification of triple phase boundary network shown with an example LSM-YSZ composite cathode sample. (a) The LSM (electronic conductor) and YSZ (ionic conductor) volume models are displayed (red and yellow, respectively; *color online*) with the TPB network visible at the boundaries; (b) the YSZ volume model has been removed, leaving just the LSM and the TPB network colored by their electrochemical classifications: active (green), inactive (red), and unknown (yellow) (c) volume model of LSM network, colored by connected component activity, revealing how the connectivity of the LSM components determines the TPB activity due to its limited percolation in this sample. The displayed volume is a limited sub-sample of an overall FIB-*nt* acquisition (sub-volume is approximately  $6 \times 10 \times 9 \mu\text{m}$ ). (For interpretation of the references to color in this figure legend, the reader is referred to the web version of this article.)

proportion of the TPB network is expected to be isolated from any larger percolated phase network, and because of this will not contribute to useful ionic, electronic, or gas conduction. Thus, it is useful to determine the active vs. inactive  $L_{\text{TPB}}$ , in addition to the total length. The present techniques and definitions used to determine TPB activity have been proposed in prior works [32,33], and have been incorporated into the  $L_{\text{TPB}}$  algorithm presented in Section 3.4.2.

Briefly, once the overall TPB network has been calculated, it is analyzed for activity by examining the connectivity of the phases (referred to as *connected components* or CC) to which it is connected. The connectivity of adjacent voxels is restricted to only those that share at least one face, meaning each voxel has a possibility of six nearest neighbors. Each CC is classified as either *percolated*, *isolated*, or *dead-end*, depending on which boundaries of the volume it intersects. A *percolated* CC is one that extends to two or more of the sampled volume's faces. This is a necessary approximation since only a limited volume of the total sample can be examined through FIB-*nt*, a *percolated* CC is assumed to be well-connected to the overall sample volume. A *dead-end* CC is one that borders just one face of and ends within the sampled volume. An *isolated* CC is one that is contained completely within the sampled volume, and has no intersections with the volume boundaries. An example of this classification process is shown in Fig. 11 for a sample SOFC cathode volume. In this sample the pore and YSZ phases were almost completely percolated, meaning the performance of the sample was limited by electronic conduction and the LSM phase determined the overall activity of the TPB network. Fig. 11c shows the CC evaluation for the LSM phase, with green, yellow, and red representing active, unknown, and inactive classifications, respectively.

Once the CC have been classified, each TPB edge is categorized based on the classes of the four voxels that it connects. An *inactive* TPB edge is one that contacts any voxel of an isolated CC. A TPB edge is *unknown* if it does not contact any isolated CC, but does contact at least one dead-end CC, and an *active* TPB edge is one that contacts only percolated CC. The total TPB network comprises multiple TPB paths that each are a set of connected TPB edges. Each TPB path is classified based upon the edges it contains. A path is *active* if all edges are active, *unknown* if all edges are either active or unknown, and *inactive* if any edges are inactive. Finally, since the ratio between the active and inactive  $L_{\text{TPB}}$  is assumed to be accurate even with the presence of unknown TPBs, the final active  $L_{\text{TPB}}$  is figured as:

$$L_{\text{TPB,A}} = A \left( 1 + \frac{U}{A+I} \right) \quad (7)$$

**Table 2**

Detailed FIB-*nt* reconstruction parameters of the composite LSM-YSZ cathode sample shown in Fig. 12. Voxel dimensions are in nm; Bounding box dimensions are in  $\mu\text{m}$ .

Total volume	Voxel size			Bounding box		
	x	y	z	x	y	z
6359.3 $\mu\text{m}^3$	19.5	24.7	20.0	26.4	19.9	12.1

where  $A$ ,  $U$ , and  $I$  are the active, unknown, and inactive  $L_{\text{TPB}}$  values initially calculated, respectively. Dividing  $L_{\text{TPB}}$  by the sample volume gives the triple phase boundary density ( $\rho_{\text{TPB}}$ ), which can be compared between samples. Finally, the fractions of the TPB network that are active and inactive ( $f_{a, \text{TPB}}$  and  $f_{i, \text{TPB}}$ ) can be compared.

#### 4. Results and discussion

To demonstrate the implementation of the methods from Sections 2 and 3, a FIB-*nt* analysis was performed on the SOFC sample described in Section 2.1. Details of the reconstruction are provided in Fig. 12 and Table 2. The sample volume was sliced at a nominal  $z$  resolution of 20 nm. The smallest average particle diameter was for the YSZ phase (715 nm), meaning this slice thickness well exceeds the minimum 10 slice per particle standard that has been proposed for FIB/SEM reconstructions [14]. The actual thickness of the slices were verified after acquisition through geometric analysis of fiducial markers [38], and were found to remain within approximately 5% of the nominal value. As such, uniform thicknesses in the  $z$  direction were assumed in order to simplify the subsequent numerical operations.  $x$ - $y$  pixel resolutions were close to 20 nm to provide approximately cubic voxels.

To gain an understanding of the statistical significance of the microstructural quantifications, a subsampling technique was used to measure the variance of each parameter throughout the collected volume. Each quantification was repeated 400 times on smaller ( $4 \times 4 \times 4 \mu\text{m}^3$ ) volumes extracted from random locations within the cathode volume. Based on these data populations, a percentile bootstrap algorithm was used to estimate the 95% confidence intervals of their means [76,77], providing a measure of the error inherent in each microstructural quantification.

The results of the FIB-*nt* reconstruction are presented in Table 3, presented in categories aligned with the parameters described in each subsection of Section 3.

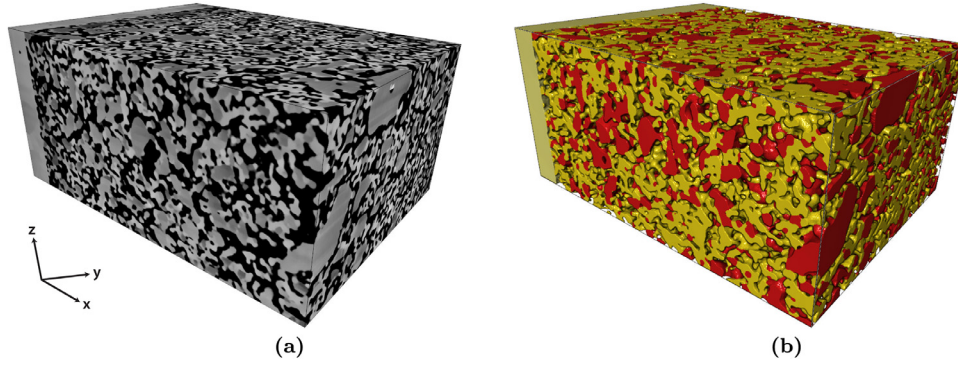


**Fig. 12.** Results from the FIB-nt acquisition and reconstruction process on an LSM-YSZ composite SOFC cathode. (a) Three-dimensional view of the acquired SEM images (Pore – black, LSM – mid-gray, YSZ – bright gray) and (b) reconstruction into a 3D volume model after image preprocessing and segmentation (Pore – not shown, LSM – red, YSZ – yellow). Dimensions of the volume are (26.4, 19.9, 12.1)  $\mu\text{m}$ . (For interpretation of the references to color in this figure legend, the reader is referred to the web version of this article.)

**Table 3**

Detailed FIB-nt reconstruction results for the composite LSM-YSZ cathode sample shown in Fig. 12. Microstructural parameters are discussed in the text, and their symbols reviewed below the table.

VOLUME AND SURFACE							
$\eta(\%)$ :	LSM	YSZ	Pore	$\bar{d}$ (nm):	LSM	YSZ	Pore
	$24.2 \pm 0.5$	$35.1 \pm 0.4$	$40.7 \pm 0.3$		$940 \pm 10$	$715 \pm 3$	$798 \pm 4$
$\nabla\eta$ ( $\%/\mu\text{m}$ ):	$x$	$5.8 \times 10^{-2}$	$2.9 \times 10^{-2}$	$-8.7 \times 10^{-2}$	SA:V	LSM	YSZ
	$y$	$1.9 \times 10^{-2}$	$-2.0 \times 10^{-1}$	$1.8 \times 10^{-1}$	( $\mu\text{m}^{-1}$ ):	$6.4 \pm 0.1$	$8.4 \pm 0.1$
	$z$	$-1.8 \times 10^{-4}$	$2.1 \times 10^{-1}$	$-2.1 \times 10^{-1}$			Pore
							$7.5 \pm 0.1$
$\eta_{\text{solid}}(\%)$ :	LSM	YSZ					
Actual	$40.9 \pm 0.7$	$59.1 \pm 0.7$					
Expected	47.6	52.4					
CONNECTIVITY STATISTICS							
$\rho_E$ ( $\mu\text{m}^{-3}$ ):	LSM	YSZ	Pore	$p$ :	LSM	YSZ	Pore
	$0.6 \pm 0.1$	$6 \pm 1$	$7 \pm 1$		0.65	1.00	1.00
$\rho_N$ ( $\mu\text{m}^{-3}$ ):	$0.7 \pm 0.1$	$4.2 \pm 0.6$	$4.8 \pm 0.7$	$\bar{L}$ (nm):	$1010 \pm 20$	$888 \pm 4$	$896 \pm 5$
$\bar{k}$ :	$1.7 \pm 0.2$	$3.0 \pm 0.1$	$3.06 \pm 0.06$				
TORTUOSITY							
$\tau$ :	LSM	YSZ	Pore	$\eta/\tau$ :	LSM	YSZ	Pore
$x$	$1.30 \pm 0.04$	$1.054 \pm 0.002$	$1.024 \pm 0.001$	$x$	$0.19 \pm 0.05$	$0.33 \pm 0.04$	$0.40 \pm 0.03$
$y$	$1.42 \pm 0.07$	$1.050 \pm 0.002$	$1.024 \pm 0.001$	$y$	$0.17 \pm 0.04$	$0.33 \pm 0.04$	$0.40 \pm 0.03$
$z$	$1.48 \pm 0.05$	$1.065 \pm 0.003$	$1.038 \pm 0.001$	$z$	$0.16 \pm 0.04$	$0.33 \pm 0.04$	$0.39 \pm 0.03$
TRIPLE PHASE BOUNDARIES							
$L_{\text{TPB}}$ ( $\mu\text{m}$ ):	Total	Active	Inactive	$f_{a, \text{TPB}}$ :	$0.50 \pm 0.01$		
	22,490	11,175	11,315	$f_{i, \text{TPB}}$ :	$0.50 \pm 0.01$		
$\rho_{\text{TPB}}$ ( $\mu\text{m}^{-2}$ ):	$3.9 \pm 0.1$	$1.94 \pm 0.08$	$1.97 \pm 0.08$				
$\eta$	phase fraction	$\rho_{E, N}$	skeleton edge/node density	$\eta/\tau$	phase fraction to tortuosity ratio		
$\nabla\eta$	phase distribution gradient	$\bar{k}$	average node degree				
$\eta_{\text{solid}}$	solid phase fraction	$p$	degree of percolation	$L_{\text{TPB}}$	TPB length		
$\bar{d}$	average particle size	$\bar{L}$	mean topological length	$\rho_{\text{TPB}}$	TPB density		
SA:V	surface area to volume ratio	$\tau$	geometric tortuosity	$f_{a, \text{TPB}}$	activity fraction		

#### 4.1. Volume quantifications

The volume fractions ( $\eta$ ) of the three phases reveal a volume porosity of approximately 41%, slightly lower than has been reported previously for LSM-YSZ cathode layers [33]. This value of 41% was found to be consistent with multiple other samples investigated (but not reported) in this work, providing confidence in the lower result.

The phase fraction gradients ( $\nabla\eta$ ) reveal little change in the cathode regardless of direction. The values found for  $\nabla\eta$  indicate a total change of  $\approx 1\%$  over the entire cathode thickness ( $x$  direction), suggesting there is no significant change in volume fraction at the length scales examined in this study.

The solid phase fractions provide information about the ratio of electronic to ionic conductor (LSM to YSZ), and whether any significant change from the expected ratio has manifested in the reconstruction. Given a 50/50 wt% mixture of the source materi-

als, a volume ratio of 47.6/52.4 would be expected for LSM/YSZ if no substantial change has occurred. The results in Table 3 indicate a significant deviation from this ratio, implying (most likely) that a chemical change has occurred, causing more material to appear brighter and to be classified as YSZ.

From average particle size  $\bar{d}$  determinations, the LSM particles were found to be significantly larger than those of the YSZ and the pore phase, and their sizes show reasonable agreement with the nominal particle diameters of 900 nm for LSM and 600 nm for YSZ. Likewise, the LSM had a significantly lower surface area to volume ratio (SA:V), suggesting these particles are overall smoother, with less corrugation in the surface.

#### 4.2. Phase connectivity

Results from the quantification of the phase skeletons reveal a significant difference between the connectivity of the LSM and the

YSZ phases in the present sample. The density of skeleton edges ( $\rho_E$ ) and nodes ( $\rho_N$ ) are drastically lower in the LSM than in either the YSZ or pore phase, meaning it is a simpler phase structure that can be described with fewer network components. Likewise, the average node degree ( $\bar{k}$ ) is correspondingly lower in LSM, suggesting lower connectivity in the phase. The degree of percolation ( $p$ ) indicates that the LSM is poorly connected throughout the volume (compared to complete percolation of YSZ and the pore), and reveals that restricted electronic transport through the LSM will limit performance of the device. Similarly, the average topological length ( $\bar{L}$ ) is longest for LSM due to its larger particles with fewer branching points. All of the connectivity statistics are effectively identical between the YSZ and pore networks, suggesting that these values may be common for all fully-percolated phases.

#### 4.3. Tortuosity

The results for tortuosity ( $\tau$ ) once again reveal LSM as the transport limiting phase. Due to its poor connectivity, there was often a lack of continuous pathway in the LSM throughout the entire sample volume, leading to significantly higher values of  $\tau$  and correspondingly higher uncertainties. Within each phase, there is little change with respect to direction of calculation, demonstrating the isotropic nature of  $\tau$  in this sample. There is a slight increase in  $\tau$  values in the  $z$  direction, which is primarily attributed to the shorter length sampled in that dimension compared to the others (12.1  $\mu\text{m}$  vs.  $\sim 20\mu\text{m}$ ). This reduced length limits the size of  $L_E$  in Eq. (4), which will lead to larger values of  $\tau$  (see Fig. 7d). The conclusions from measurements of  $\tau$  are affirmed when considering the phase fraction to tortuosity ratio ( $\eta/\tau$ ). This parameter is expected to be proportional to the effective diffusivity (Eq. (5)) and provides a more intuitive insight into how the geometry of a phase will affect its transport properties. Again, isotropic values are obtained, with LSM having the lowest  $\eta/\tau$  of the three phases, yielding reduced conduction through this phase.

#### 4.4. Triple phase boundaries

The total density of triple phase boundary points ( $\rho_{\text{TPB}}$ ) for this sample was found to be  $3.9 \pm 0.1 \mu\text{m}^{-2}$ . Prior theoretical studies regarding the dependence of  $\rho_{\text{TPB}}$  on particle size and  $\eta$  indicate that a value in the range of  $2 \mu\text{m}^{-2}$  to  $6 \mu\text{m}^{-2}$  would be expected for the microstructure measured in this work [74]. This indicates the  $\rho_{\text{TPB}}$  calculation algorithm introduced here produces results that can be directly compared with other studies.

Both the total  $\rho_{\text{TPB}}$  and the active fraction are significantly dependent on the initial particle size of the source material and the specific sintering conditions (which control final particle size) [78]. The active fraction of the TPB network ( $f_{a, \text{TPB}}$ ) was found to be 50% for this sample. Results from a similar LSM-YSZ cathode measured by Wilson et al. [33] have found higher  $f_{a, \text{TPB}}$  values (67%), but their study reconstructed a total cathode volume of only  $685 \mu\text{m}^3$  (about one-tenth of that studied in this work), suggesting that the limited volume may artificially inflate measurements of  $f_{a, \text{TPB}}$ , due to the definition of activity being dependent on edge connectivity. This result underscores the importance of collecting a sufficiently large volume for accurate quantification.

### 5. Conclusions

FIB-*nt* is a remarkably powerful technique for measuring material microstructures, and is applicable to wide range of sample types. Analyses of “advanced” microstructural properties such as tortuosity and triple phase boundary length are of great interest when it comes to determining the behavior of many material systems, but are difficult to quantify with currently available commer-

cial and open-source tools. Additionally, specific implementations from research are rarely made available to the community, leading to severe discrepancies between reported methods.

This work has introduced and provided an overview of a number of techniques that can be used to process FIB-*nt* data and quantify the microstructural properties of a reconstructed volume. Significant advancements have been presented in the correction of the common FIB-shading artifact, allowing for improved segmentations. Additional improvements in the calculation of microstructural parameters have been presented, in particular for tortuosity and triple phase boundaries. The implementations introduced in this work have been made available for public use in an online code repository, with the intent of allowing peer-review of not only results, but methodology as well [30].

Examples of the calculations discussed in this work have been reported for an LSM-YSZ SOFC composite cathode layer. The results are largely in line with prior reports on this system, with the most significant variation apparent in  $\eta_{\text{solid}}$  and  $f_{a, \text{TPB}}$ . These calculations revealed LSM as the transport-limiting phase in this cell, due to its high tortuosity and poor connectivity. These results demonstrate a baseline quantification for the LSM-YSZ system, and provide a common and open methodological framework that can be easily extended to future FIB-*nt* reconstructions in a wide range of material systems.

#### Disclaimer

Commercial materials and products identified in this article are not intended to imply recommendation or endorsement by the National Institute of Standards and Technology, nor is the intention of this article to imply that the materials identified are necessarily the best available for the stated purpose.

#### Acknowledgments

This project was funded by the US Department of Energy under NETL Contract DEFE0009084, and JAT acknowledges support under the NSF Graduate Research Fellowship Program, Grant no. DGE1322106. The authors thank John Hagedorn (Information Technology Laboratory at the National Institute of Standards and Technology) for extensive assistance in development and implementation of the TPB calculation algorithm, as well as Shuo Wang (Trane Intelligent Services) for conversations inspiring the FIB/SEM shading correction scheme. The authors also thank Joshua Schumacher at the Center of Nanoscale Science and Technology (at NIST) for training and assistance with FIB/SEM and useful discussions.

#### References

- [1] B. Inkson, M. Mulvihill, G. Möbus, 3D determination of grain shape in a FeAl-based nanocomposite by 3D FIB tomography, *Scr. Mater.* 45 (2001) 753–758.
- [2] FEI Company, Auto Slice & View, for Automated Acquisition of High Resolution 3d Images, 2016, (<http://www.fei.com/software/auto-slice-and-view/>). (Accessed on 06/03/2016).
- [3] Zeiss, Atlas 5 – Large Area Imaging for ZEISS SEM, FE-SEM & FIB-SEM, 2016, ([http://www.zeiss.com/microscopy/en\\_us/products/microscope-software/atlas-5.html](http://www.zeiss.com/microscopy/en_us/products/microscope-software/atlas-5.html)). (Accessed on 06/03/2016).
- [4] Hitachi High Technologies, NanoDUE™ FIB-SEM NB5000, 2016, ([http://www.hitachi-hightech.com/us/product\\_detail/?pn=em-nb5000](http://www.hitachi-hightech.com/us/product_detail/?pn=em-nb5000)). (Accessed on 06/03/2016).
- [5] TESCAN, 3d Tomography, 2016, (<http://www.tescan.com/en/other-products/software/3d-tomography>). (Accessed on 06/03/2016).
- [6] L. Holzer, M. Cantoni, Review of FIB tomography, Nanofabrication using Focused Ion and Electron Beams: Principles and Applications, Oxford University Press, 2012, pp. 410–435. URL [http://books.google.de/books?id=U-0mwQcHX5YC&dq=Review+of+FIB-tomography+Lorenz+Holzer&hl=de&source=gbs\\_navlinks\\_s](http://books.google.de/books?id=U-0mwQcHX5YC&dq=Review+of+FIB-tomography+Lorenz+Holzer&hl=de&source=gbs_navlinks_s).
- [7] M. Schaffer, J. Wagner, B. Schaffer, M. Schmied, H. Mulders, Automated three-dimensional X-ray analysis using a dual-beam FIB, *Ultramicroscopy* 107 (2007) 587–597, doi:10.1016/j.ultramic.2006.11.007.

- [8] J. Guyon, N. Gey, D. Goran, S. Chalal, F. Pérez-Willard, Advancing FIB assisted 3D EBSD using a static sample setup, *Ultramicroscopy* 161 (2016) 161–167, doi:10.1016/j.ultramic.2015.11.011.
- [9] P. Burdet, J. Vannod, A. Hessler-Wyser, M. Rappaz, M. Cantoni, Three-dimensional chemical analysis of laser-welded NiTi-stainless steel wires using a dual-beam FIB, *Acta Mater.* 61 (8) (2013) 3090–3098, doi:10.1016/j.actamat.2013.01.069.
- [10] T. Prill, K. Schladitz, D. Jeulin, M. Faessel, C. Wieser, Morphological segmentation of FIB-SEM data of highly porous media, *J. Microsc.* 250 (2) (2013) 77–87, doi:10.1111/jmi.12021.
- [11] B. Bai, M. Elgmati, H. Zhang, M. Wei, Rock characterization of Fayetteville shale gas plays, *Fuel* 105 (2013) 645–652, doi:10.1016/j.fuel.2012.09.043. ISSN 00162361, URL <http://linkinghub.elsevier.com/retrieve/pii/S0016236112007569>.
- [12] J.A. Taillon, C. Pellegrinelli, Y. Huang, E. Wachsmann, L. Salamanca-Riba, Three dimensional microstructural characterization of cathode degradation in SOFCs using FIB/SEM and TEM, *Microsc. Microanal.* 21 (S3) (2015) 2161–2162. URL <http://journals.cambridge.org/action/displayAbstract?fromPage=online&aid=9916717>.
- [13] D. Gostovic, N.J. Vito, K.A. O'Hara, K.S. Jones, E.D. Wachsmann, Microstructure and connectivity quantification of complex composite solid oxide fuel cell electrode three-dimensional networks, *J. Am. Ceram. Soc.* 94 (2) (2011) 620–627, doi:10.1111/j.1551-2916.2010.04111.x. ISSN 00027820.
- [14] L. Holzer, F. Indutnyi, P.H. Gasser, B. Münch, M. Wegmann, Three-dimensional analysis of porous BaTiO<sub>3</sub> ceramics using FIB nanotomography, *J. Microsc.* 216 (Pt 1) (2004) 84–95, doi:10.1111/j.0022-2720.2004.01397.x. ISSN 0022-2720, <http://www.ncbi.nlm.nih.gov/pubmed/15369488>.
- [15] L. Holzer, B. Münch, M. Wegmann, P.H. Gasser, R.J. Flatt, FIB-nanotomography Of particulate systems – Part I: Particle shape and topology of interfaces, *J. Am. Ceram. Soc.* 89 (8) (2006) 2577–2585, doi:10.1111/j.1551-2916.2006.00974.x. ISSN 0002-7820.
- [16] J.R. Wilson, W. Kobsiriphat, R. Mendoza, H.-Y. Chen, J.M. Hiller, D.J. Miller, K. Thornton, P.W. Voorhees, S.B. Adler, S.A. Barnett, Three-dimensional reconstruction of a solid-oxide fuel-cell anode, *Nat. Mater.* 5 (7) (2006), doi:10.1038/nmat1668. 4–541, ISSN 1476-1122, URL <http://www.ncbi.nlm.nih.gov/pubmed/16767095>.
- [17] R.K. Bansal, A. Kubis, R. Hull, J.M. Fitz-Gerald, High-resolution three-dimensional reconstruction: a combined scanning electron microscope and focused ion-beam approach, *J. Vac. Sci. Technol. B* 24 (2) (2006) 554, doi:10.1116/1.2167987. ISSN 10711023, URL <http://link.aip.org/link/JVTBD9v24/i2/p554/s1&Agg=doi>.
- [18] D. Gostovic, J.R. Smith, D.P. Kundinger, K.S. Jones, E.D. Wachsmann, Three-dimensional reconstruction of porous LSCF cathodes, *Electrochem. Solid-State Lett.* 10 (12) (2007) B214, doi:10.1149/1.2794672. ISSN 10990062, URL <http://link.aip.org/link/ESLEF6/v10/i12/pB214/s1&Agg=doi>.
- [19] J.R. Smith, A. Chen, D. Gostovic, D. Hickey, D.P. Kundinger, K. Duncan, R. DeHoff, K.S. Jones, E.D. Wachsmann, Evaluation of the relationship between cathode microstructure and electrochemical behavior for SOFCs, *Solid State Ionics* 180 (1) (2009) 90–98, doi:10.1016/j.ssi.2008.10.017. ISSN 01672738, URL <http://linkinghub.elsevier.com/retrieve/pii/S016727380800619X>.
- [20] D. Gostovic, K.A. O'Hara, N.J. Vito, E.D. Wachsmann, K.S. Jones, Multiple length scale characterization of doped lanthanum manganate composite cathodes, *Electrochem. Soc. Trans.* 16 (51) (2009) 83–93.
- [21] N. Shikazono, D. Kanno, K. Matsuzaki, H. Teshima, S. Sumino, N. Kasagi, Numerical assessment of SOFC anode polarization based on three-dimensional model microstructure reconstructed from FIB-SEM images, *J. Electrochem. Soc.* 157 (5) (2010) B665, doi:10.1149/1.3330568. ISSN 00134651, URL <http://jes.ecsdl.org/cgi/doi/10.1149/1.3330568>.
- [22] H. Iwai, N. Shikazono, T. Matsui, H. Teshima, M. Kishimoto, R. Kishida, D. Hayashi, K. Matsuzaki, D. Kanno, M. Saito, H. Muroyama, K. Eguchi, N. Kasagi, H. Yoshida, Quantification of SOFC anode microstructure based on dual beam FIB-SEM technique, *J. Power Sources* 195 (4) (2010) 955–961, doi:10.1016/j.jpowsour.2009.09.005. ISSN 03787753, URL <http://linkinghub.elsevier.com/retrieve/pii/S0378775309015456>.
- [23] J. Joos, T. Carraro, A. Weber, E. Ivers-Tiffée, Reconstruction of porous electrodes by FIB/SEM for detailed microstructure modeling, *J. Power Sources* 196 (17) (2011) 7302–7307, doi:10.1016/j.jpowsour.2010.10.006. ISSN 03787753, URL <http://linkinghub.elsevier.com/retrieve/pii/S0378775310017337>.
- [24] N. Vivet, S. Chupin, E. Estrade, T. Piquero, P. Pommier, D. Rochais, E. Bruneton, 3D Microstructural characterization of a solid oxide fuel cell anode reconstructed by focused ion beam tomography, *J. Power Sources* 196 (18) (2011) 7541–7549, doi:10.1016/j.jpowsour.2011.03.060. ISSN 03787753, URL <http://linkinghub.elsevier.com/retrieve/pii/S0378775311006756>.
- [25] G.A. Hughes, K. Yakal-Kremeski, A.V. Call, S.A. Barnett, Durability testing of solid oxide cell electrodes with current switching, *J. Electrochem. Soc.* 159 (12) (2012) F858–F863, doi:10.1149/2.008301jes. ISSN 0013-4651.
- [26] K.T. Lee, N.J. Vito, E.D. Wachsmann, Comprehensive quantification of Ni-Gd<sub>0.1</sub>Ce<sub>0.9</sub>O<sub>1.95</sub> anode functional layer microstructures by three-dimensional reconstruction using a FIB/SEM dual beam system, *J. Power Sources* 228 (2013) 220–228, doi:10.1016/j.jpowsour.2012.11.117. ISSN 03787753, URL <http://linkinghub.elsevier.com/retrieve/pii/S0378775312018022>.
- [27] K. Yakal-Kremeski, J.S. Cronin, Y.-C. K. Chen-Wiegart, J. Wang, S.A. Barnett, Studies of solid oxide fuel cell electrode evolution using 3D tomography, *Fuel Cells* 13 (4) (2013) 449–454, doi:10.1002/fuce.201200177. ISSN 16156846.
- [28] J. Joos, M. Ender, I. Rotscholl, N.H. Menzler, E. Ivers-Tiffée, Quantification of double-layer Ni/YSZ fuel cell anodes from focused ion beam tomography data, *J. Power Sources* 246 (2014) 819–830, doi:10.1016/j.jpowsour.2013.08.021. ISSN 03787753, URL <http://linkinghub.elsevier.com/retrieve/pii/S0378775313013608>.
- [29] H.G. Jones, K.P. Mingard, D.C. Cox, Investigation of slice thickness and shape milled by a focused ion beam for three-dimensional reconstruction of microstructures, *Ultramicroscopy* 139 (2014) 20–28, doi:10.1016/j.ultramic.2014.01.003. ISSN 18792723, URL <http://linkinghub.elsevier.com/retrieve/pii/S0304399114000138>.
- [30] J.A. Taillon, Advanced Analytical Microscopy at the Nanoscale: Applications in Wide Bandgap and Solid Oxide Fuel Cell Materials – FIB-nt Code Repository, University of Maryland, College Park, 2016 Ph.D. thesis. doi:10.13016/M29806
- [31] N.Q. Minh, T. Takahashi, Science and Technology of Ceramic Fuel Cells, Elsevier, Amsterdam, 1995, doi:10.1016/B978-0-44489568-4/50002-5. ISBN 9780444895684, URL <http://www.sciencedirect.com/science/article/pii/B9780444895684500025>.
- [32] J.R. Wilson, M. Gameiro, K. Mischaikow, W. Kalies, P.W. Voorhees, S.A. Barnett, Three-dimensional analysis of solid oxide fuel cell Ni-YSZ anode interconnectivity, *Microsc. Microanal.* 15 (1) (2009a) 71, doi:10.1017/S13431927609090096. ISSN 1431-9276, URL <http://www.ncbi.nlm.nih.gov/pubmed/19144260>.
- [33] J.R. Wilson, A.T. Duong, M. Gameiro, H.-Y. Chen, K. Thornton, D.R. Mumm, S.A. Barnett, Quantitative three-dimensional microstructure of a solid oxide fuel cell cathode, *Electrochem. Commun.* 11 (5) (2009b) 1052–1056, doi:10.1016/j.elecom.2009.03.010. ISSN 13882481, URL <http://linkinghub.elsevier.com/retrieve/pii/S1388248109001192>.
- [34] C.J. Gommers, A.J. Bons, S. Blacher, J.H. Dunsmuir, A.H. Tsou, Practical methods for measuring the tortuosity of porous materials from binary or gray-tone tomographic reconstructions, *AIChE J.* 55 (8) (2009) 2000–2012, doi:10.1002/aic.11812. ISSN 00011541.
- [35] B. Münch, P. Trtik, F. Marone, M. Stampanoni, Stripe and ring artifact removal with combined wavelet-Fourier filtering, *Opt. Express* 17 (10) (2009) 8567, doi:10.1364/OE.17.008567. ISSN 1094-4087, URL <http://www.ncbi.nlm.nih.gov/pubmed/19434191> <http://www.opticsinfobase.org/abstract.cfm?URI=oe-17-10-8567>.
- [36] D.C. Joy, Control of charging in low-voltage SEM, *Scanning* 11 (1989) 1–4, doi:10.1002/sca.4950110102. ISSN 01610457, URL <http://onlinelibrary.wiley.com/doi/10.1002/sca.4950110102/abstract>.
- [37] K.L. Willis, A.B. Abell, D.A. Lange, Image-based characterization of cement pore structure using wood metal intrusion, *Cem. Concr. Res.* 28 (12) (1998) 1695–1705, doi:10.1016/S0008-8846(98)00159-8. ISSN 00088846, URL <http://linkinghub.elsevier.com/retrieve/pii/S0008884698001598>.
- [38] E. Principe, Patent, US 8178838, 2012, URL <https://www.google.com/patents/US8178838>.
- [39] J. Schindelin, I. Arganda-Carreras, E. Frise, V. Kaynig, M. Longair, T. Pietzsch, S. Preibisch, C. Rueden, S. Saalfeld, B. Schmid, J.-Y. Tinevez, D.J. White, V. Hartenstein, K. Eliceiri, P. Tomancak, A. Cardona, Fiji: an open-source platform for biological-image analysis, *Nat. Methods* 9 (7) (2012) 676–682, doi:10.1038/nmeth.2019.
- [40] S. van der Walt, S.C. Colbert, G. Varoquaux, The NumPy array: a structure for efficient numerical computation, *Comput. Sci. Eng.* 13 (2) (2011) 22–30, doi:10.1109/mcse.2011.37.
- [41] G. Bradski, OpenCV Computer Vision Library, Dr. Dobb's J. Softw. Tools (2000). URL <http://www.drdoobs.com/open-source/the-opencv-library/184404319>.
- [42] S. van der Walt, J.L. Schönberger, J. Nunez-Iglesias, F. Boulogne, J.D. Warner, N. Yager, E. Gouillart, T. Yu, The scikit-image contributors, scikit-image: image processing in Python, *PeerJ* 2 (2014) e453, doi:10.7717/peerj.453. ISSN 2167-8359.
- [43] P. Thévenaz, U. Ruttimann, M. Unser, A pyramid approach to subpixel registration based on intensity, *IEEE Trans. Image Process.* 7 (1) (1998) 27–41.
- [44] M. Schaffer, J. Wagner, Block lift-out sample preparation for 3D experiments in a dual beam focused ion beam microscope, *Microchim. Acta* 161 (3–4) (2008) 421–425, doi:10.1007/s00604-007-0853-5. ISSN 00263672.
- [45] X. Dai, The effects of image misregistration on the accuracy of remotely sensed change detection, *IEEE Trans. Geosci. Remote Sens.* 36 (5) (1998) 1566–1577, doi:10.1109/36.718860. ISSN 01962892, URL <http://ieeexplore.ieee.org/lpdocs/epic03/wrapper.htm?arnumber=718860>.
- [46] A. Buades, B. Coll, J.-M. Morel, A non-local algorithm for image denoising, in: Proceedings of the 2005 IEEE Computer Society Conference on Computer Vision and Pattern Recognition, CVPR'05, vol. 2, IEEE, 2005, pp. 60–65, doi:10.1109/CVPR.2005.38. ISBN 0-7695-2372-2, URL <http://ieeexplore.ieee.org/lpdocs/epic03/wrapper.htm?arnumber=1467423>.
- [47] A. Buades, B. Coll, J.-M. Morel, Non-local means denoising, *Image Process. On Line* 1 (2011) 490–530, doi:10.5201/ipl.2011.bcm\_nlm. URL [http://www.ipol.im/pub/art/2011/bcm\\_nlm/](http://www.ipol.im/pub/art/2011/bcm_nlm/).
- [48] OpenCV Developers, Image Denoising, 2016. [http://docs.opencv.org/master/d5/d69/tutorial\\_py\\_non\\_local\\_means.html](http://docs.opencv.org/master/d5/d69/tutorial_py_non_local_means.html).
- [49] L. Vincent, P. Soille, Watersheds in digital spaces: an efficient algorithm based on immersion simulations, *IEEE Trans. Pattern Anal. Mach. Intell.* 13 (6) (1991) 583–598. ISSN 01628828, doi:10.1109/34.87344, URL <http://ieeexplore.ieee.org/lpdocs/epic03/wrapper.htm?arnumber=87344>.
- [50] Y. Chen, J.Z. Wang, Image categorization by learning and reasoning with regions, *J. Mach. Learn. Res.* 5 (2004) 913–939. ISSN 15324435, URL <http://portal.acm.org/citation.cfm?id=1005332.1016789>.
- [51] J. Shotton, M. Johnson, R. Cipolla, Semantic texton forests for image categorization and segmentation, in: Proceedings of the 26th IEEE Conference on Computer Vision and Pattern Recognition, CVPR ISSN 1063-6919, 2008, doi:10.1109/CVPR.2008.4587503.

- [52] M. Rastgarpour, J. Shanbehzadeh, Application of AI techniques in medical image segmentation and novel categorization of available methods and tools, in: *Proceedings of the International Multi Conference of Engineers and Computer Scientists, IMECS, 2011, Hong Kong, 1, 2011*, pp. 1–6.
- [53] Y. Artan, Interactive image segmentation using machine learning techniques, in: *Proceedings of Canadian Conference on Computer and Robot Vision, 2011*, pp. 264–269, doi:10.1109/CRV.2011.42.
- [54] Blender Online Community, Blender – A 3D Modelling and Rendering Package, Blender Foundation, Blender Institute, Amsterdam, 2016. URL <http://www.blender.org>.
- [55] W. Schroeder, K. Martin, B. Lorensen, Visualization Toolkit: An Object-Oriented Approach to 3D Graphics, fourth ed., Kitware, 2006. ISBN 193093419X, URL <https://books.google.com/books?id=rx4vPwAACAAJ&dq=isbn:9781930934191&hl=en&sa=X&ved=0ahUKewijmdXc27bLAhWLHh4KH4YhuAB8Q6AEIHTAA>.
- [56] S. Brunauer, P.H. Emmett, E. Teller, Adsorption of gases in multimolecular layers, *J. Am. Chem. Soc.* 60 (2) (1938) 309–319, doi:10.1021/ja01269a023. ISSN 00027863.
- [57] J.A. Taillon, C. Pellegrinelli, Y. Huang, E.D. Wachsman, L.G. Salamanca-Riba, Three dimensional microstructural characterization of cathode degradation in SOFCs using focused ion beam and SEM, *ECS Trans.* 61 (1) (2014) 109–120, doi:10.1149/06101.0109ecst. URL <http://ecst.ecsdl.org/content/61/1/109.abstract>.
- [58] P.K. Saha, G. Borgfors, G. Sanniti di Baja, A survey on skeletonization algorithms and their applications, *Pattern Recognit. Lett.* 76 (2016) 312, doi:10.1016/j.patrec.2015.04.006. ISSN 01678655, URL <http://www.sciencedirect.com/science/article/pii/S0167865515001233>.
- [59] C. Pudney, Distance-ordered homotopic thinning: a skeletonization algorithm for 3D digital images, *Comput. Vis. Image Underst.* 72 (3) (1998) 404–413, doi:10.1006/cviu.1998.0680. ISSN 10773142, URL <http://linkinghub.elsevier.com/retrieve/pii/S1077314298906804>.
- [60] C. Fouard, G. Malandain, S. Prohaska, M. Westerhoff, F. Cassot, C. Mazel, D. Asselot, J. Marc-Vergnes, Skeletonization by blocks for large 3D datasets: application to brain microcirculation, in: *Proceedings of the 2004 2nd IEEE International Symposium on Biomedical Imaging: Macro to Nano (IEEE Cat No. 04EX821)*, vol. 2, IEEE, 2004, pp. 89–92, doi:10.1109/ISBI.2004.1398481. ISBN 0-7803-8388-5, URL <http://ieeexplore.ieee.org/lpdocs/epic03/wrapper.htm?arnumber=1398481>.
- [61] H.J. Johnson, M. McCormick, L. Ibáñez, T.I.S. Consortium, *The ITK Software Guide*, third ed., Kitware, Inc., 2013. URL <http://www.itk.org/itkSoftwareGuide.pdf>.
- [62] H. Homann, Implementation of a 3D thinning algorithm, *Insight J.* (2007). URL <http://hdl.handle.net/1926/1292>.
- [63] The CGAL Project, *CGAL User and Reference Manual*, CGAL Editorial Board, 4.7 edition, 2015. URL <http://doc.cgal.org/4.7/Manual/packages.html>.
- [64] X. Gao, S. Lorient, A. Tagliasacchi, Triangulated surface mesh skeletonization, in: *CGAL User and Reference Manual*, 4.7 ed., CGAL Editorial Board, 2015. URL <http://doc.cgal.org/4.7/Manual/packages.html#PkgMeanCurvatureSkeleton3Summary>.
- [65] M.B. Clennell, *Tortuosity: A Guide Through the Maze*, 122(1), Geological Society, London, 1997, pp. 299–344, doi:10.1144/GSL.SP.1997.122.01.18. Special Publications, ISSN 0305-8719.
- [66] G. Brus, K. Miyoshi, H. Iwai, M. Saito, H. Yoshida, Change of an anode's microstructure morphology during the fuel starvation of an anode-supported solid oxide fuel cell, *Int. J. Hydrogen Energy* (2015) 1–8, doi:10.1016/j.ijhydene.2015.03.143. ISSN 03603199, URL <http://linkinghub.elsevier.com/retrieve/pii/S0360319915007892>.
- [67] G. Gaiselmann, M. Neumann, V. Schmidt, O. Pecho, T. Hocker, L. Holzer, Quantitative relationships between microstructure and effective transport properties based on virtual materials testing, *AIChE J.* 60 (6) (2014) 1983–1999, doi:10.1002/aic.14416.
- [68] L. Holzer, O. Stenzel, O. Pecho, T. Ott, G. Boiger, M. Gorbar, Y. De Hazan, D. Penner, I. Schneider, R. Cervera, P. Gasser, Fundamental relationships between 3D pore topology, electrolyte conduction and flow properties: towards knowledge-based design of ceramic diaphragms for sensor applications, *Mater. Des.* 99 (2016) 314–327, doi:10.1016/j.matdes.2016.03.034.
- [69] O. Stenzel, O. Pecho, L. Holzer, M. Neumann, V. Schmidt, Predicting effective conductivities based on geometric microstructure characteristics, *AIChE J.* 62 (5) (2016) 1834–1843, doi:10.1002/aic.15160. ISSN 1547-5905, URL <http://dx.doi.org/10.1002/aic.15160>.
- [70] J.A. Sethian, Fast marching methods, *SIAM Rev.* 41 (2) (1999) 199–235, doi:10.1137/S0036144598347059. ISSN 0036-1445.
- [71] J. Furtney, et al., scikit-fmm: The fast marching method for Python (2012). <https://github.com/scikit-fmm/scikit-fmm>.
- [72] J.-W. Kim, A.V. Virkar, K. Fung, K. Mehta, S.C. Singhal, Polarization effects in intermediate temperature, anode-supported solid oxide fuel cells, *J. Electrochem. Soc.* 146 (1) (1999) 69, doi:10.1149/1.1391566. ISSN 00134651, URL <http://jes.ecsdl.org/cgi/doi/10.1149/1.1391566>.
- [73] H. Fukunaga, M. Ihara, K. Sakaki, K. Yamada, The relationship between overpotential and the three phase boundary length, *Solid State Ionics* 86–88 (Part 2) (1996) 1179–1185, doi:10.1016/0167-2738(96)00284-6. ISSN 01672738.
- [74] B. Kenney, M. Valdmanis, C. Baker, J. Pharoah, K. Karan, Computation of TPB length, surface area and pore size from numerical reconstruction of composite solid oxide fuel cell electrodes, *J. Power Sources* 189 (2) (2009) 1051–1059, doi:10.1016/j.jpowsour.2008.12.145. ISSN 03787753, URL <http://linkinghub.elsevier.com/retrieve/pii/S0378775309000378>.
- [75] J.R. Wilson, S.A. Barnett, Solid oxide fuel cell Ni-YSZ anodes: Effect of composition on microstructure and performance, *Electrochem. Solid-State Lett.* 11 (10) (2008) B181, doi:10.1149/1.2960528. ISSN 10990062.
- [76] B. Efron, R. Tibshirani, *An Introduction to the Bootstrap* (Chapman & Hall/CRC Monographs on Statistics & Applied Probability), Chapman and Hall/CRC, 1994. ISBN 0412042312, URL <http://www.amazon.com/Introduction-Bootstrap-Monographs-Statistics-Probability/dp/0412042312%3FSubscriptionId%3DOJYN1NW651KCA56C102%26tag%3Dteckie-20%26linkCode%3Dxm%26camp%3D2025%26creative%3D165953%26creativeASIN%3D0412042312>.
- [77] C. Evans, scikits-bootstrap: Bootstrap confidence interval algorithms for scipy, 2012, <https://github.com/cgevans/scikits-bootstrap>.
- [78] J.S. Cronin, K. Muangnapoh, Z. Patterson, K.J. Yakal-Kremiski, V.P. Dravid, S.A. Barnett, Effect of firing temperature on LSM-YSZ composite cathodes: a combined three-dimensional microstructure and impedance spectroscopy study, *J. Electrochem. Soc.* 159 (4) (2012) B385, doi:10.1149/2.053204jes.